01 Oct 2022

Mechanical Behavior of Single-Flawed Cylindrical Specimens Subjected to Axial Loading: A Numerical Investigation

Mostafa Asadizadeh

Saeed Khosravi

Javad Karimi

Taghi Sherizadeh
Missouri University of Science and Technology, sherizadeh@mst.edu

et. al. For a complete list of authors, see https://scholarsmine.mst.edu/min_nuceng_facwork/1687

Recommended Citation

M. Asadizadeh et al., "Mechanical Behavior of Single-Flawed Cylindrical Specimens Subjected to Axial Loading: A Numerical Investigation," *Bulletin of Engineering Geology and the Environment*, vol. 81, no. 10, article no. 442, Springer, Oct 2022.
The definitive version is available at https://doi.org/10.1007/s10064-022-02940-4

Bulletin of Engineering Geology and the Environment (2022) 81:442
https://doi.org/10.1007/s10064-022-02940-4

ORIGINAL PAPER

Mechanical behavior of single-flawed cylindrical specimens subjected to axial loading: a numerical investigation

Mostafa Asadizadeh[1,2] · Saeed Khosravi[3] · Javad Karimi[4] · Taghi Sherizadeh[2] · Sanaz Vajedian[5] · Mohammad Farouq Hossaini[4]

Received: 17 May 2021 / Accepted: 12 September 2022 / Published online: 23 September 2022

Abstract

Discontinuities are inherent components of rock masses and can range from fissures to large faults. Single fissures, the so-called flaws, may affect the mechanical behavior of rock mass, crack initiation, and propagation. In this paper, numerical investigations have been conducted on central-flawed cylindrical specimens subjected to axial loading to investigate the effect of flaw angle (α), length ($2a$), and aperture (A) on their mechanical behavior and crack development. Particle Flow Code (PFC3D) was adopted to investigate the cracking process of the cylindrical specimens and maximum principal stresses at flaw tips. The numerical models are calibrated and verified using extensive experimental tests. The results show that increasing α, *UCS*, and E increase while increasing $2a$ decreases *UCS* and E, and A does not affect these two parameters. Moreover, numerical simulations reveal that as α rises, the three principal stresses generally fall when $2a = 13$ and 26 mm. $\sigma 1$ and $\sigma 3$ peak at $\alpha = 45°$, and $\sigma 2$ reaches a maximum at $\alpha = 30°$ in models with $2a = 39$ mm. The cracking patterns resulting from both methods are highly consistent in that tensile cracks type 1 mainly form at $\alpha = 15°$ to 75°, and tensile cracks type 3 are dominant at other angles. Finally, it is concluded that flaw aperture scarcely affects failure patterns.

Keywords *UCS* · Modulus of elasticity · Crack development · Principal stress · Flaw tip · PFC^{3D}

Abbreviations

UCS	Unconfined compressive strength (MPa)
E	Modulus of elasticity (GPa)
σ_t	Tensile strength (MPa)
ν	Poisson's ratio
E_c	Particle modulus of elasticity (GPa)
$\overline{\lambda}$	Radius multiplier
α	Flaw inclination angle (°)
A	Flaw aperture (mm)
$2a$	Flaw length (mm)
$\overline{E_c}$	Elastic modulus of flat-joint bonds (GPa)
k_n	Normal stiffness of ball contact (N/m)
k_s	Shear stiffness of ball contacts (N/m)
R_{max}	Maximum radius of balls (mm)
R_{min}	Minimum radius of balls (mm)
$\overline{k_s}$	Shear stiffness of flat-joint bonds (N/m)
$\overline{k_n}$	Normal stiffness of flat-joint bonds (N/m)
$\sigma_{xx}, \sigma_{yy}, \sigma_{zz}, \sigma_{xy}, \sigma_{xz}, \sigma_{yz}$	Stress tensor components in global coordinate x, y, z (MPa)
$\sigma_1, \sigma_2, \sigma_3$	Principal stresses (MPa)
$\boldsymbol{n}_1, \mathrm{n}_2, \boldsymbol{n}_3$	Principal stress direction vectors
$\boldsymbol{i}, \boldsymbol{j}, \boldsymbol{k}$	Unit vectors in global coordinate x, y, z

✉ Mostafa Asadizadeh
masadizadeh@mines.edu

[1] Colorado School of Mines, 1500 Illinois St, Golden, CO 80401, USA

[2] Department of Mining and Explosives Engineering, Missouri University of Science and Technology, Rolla, MO 65409, USA

[3] Department of Mining Engineering, Shahid Bahonar University of Kerman, Kerman, Iran

[4] School of Mining Engineering, College of Engineering, University of Tehran, Tehran 1439957131, Iran

[5] Geological Sciences and Geological and Petroleum Engineering, Missouri University of Science and Technology, Rolla, MO 65409, USA

Introduction

Discontinuities, such as fissures, faults, joints, and bedding planes, are common components of rock masses (Wittke 2014). In many engineering applications, such as rock slopes, tunnels, and rock foundations, the mechanical behavior of rock masses is mainly governed by these discontinuities (Asadizadeh et al. 2018, 2019; Niu et al. 2020). Such structures can weaken the mechanical properties of rock masses, especially strength and deformability (Hoek and Martin 2014; Yin et al. 2014). Besides, it has been experimentally found that flaws in a rock specimen propagate at a microscopic scale due to the increased applied load. The crack development may cause macroscopic phenomena ranging from crack coalescence, volumetric dilation, and ductile to brittle transition (Bieniawski 1967a, b; Nemat-Nasser and Horii 1982; Horii and Nemat-Nasser 1985; Martin and Chandler 1994). Therefore, investigating the strength, deformability, and cracking processes of flawed rocks is of paramount importance to gain insight into the mechanisms leading to the fracturing of the rock mass (Yang et al. 2018; Zhao et al. 2019). This is essential to the design and stability analysis of structures constructed in or on rock masses such as slopes, tunnels, and foundations (Zhao et al. 2019). Such investigations can also result in more economical and environmentally friendly designs in rock engineering projects (Sun et al. 2019).

Several researchers have numerically investigated the effect of flaw geometry on the mechanical response of flawed specimens. Manouchehrian et al. (2014) investigated the effect of flaw inclination angle on *UCS* using PFC^{2D}. They reported that as the flaw inclination angle (α) rises, *UCS* first declines and then increases, with $\alpha = 15°$ and 75° having the lowest and highest values, respectively. Sun et al. (2019) evaluated the effect of a single flaw on the mechanical behavior of prismatic samples made of rock-like materials using PFC^{2D}. They established that with the increase of flaw inclination angle, *UCS* falls and then rises, with the lowest and highest values at $\alpha = 45°$ and 90°, respectively. They also compared the capability of two contact models in PFC^{2D}, namely flat-joint and parallel-bond models, in terms of stress state, crack initiation, propagation, and type, which indicated that the flat-joint model yields more realistic results. Lin et al. (2019) conducted numerical simulations using PFC^{2D} to evaluate the impact of flaw inclination angle on *UCS* of prismatic single-flawed specimens. The study showed that *UCS* declines at $\alpha = 15^{\circ}$, followed by an increase at $\alpha = 75°$, before experiencing a fall at $\alpha = 90°$. Shen et al. (Shen et al. 2021) conducted numerical simulations using PFC^{2D} to evaluate the effect of flaw width on the mechanical properties of single-flawed samples. They suggested that when the width is lower than 1 mm, *UCS* and *E* significantly fall with the increase of flaw width, especially for $\alpha < 60°$. Asadizadeh et al. (2022) adopted artificial intelligence methods to investigate the effect of flaw geometry on the mechanical behavior of single-flawed specimens. Their findings revealed that flaw aperture considerably influences *UCS* at lower flaw length, whereas its impact declines remarkably when flaw length rises. Additionally, at lower flaw length, stress declines at $\alpha = 45°$.

On the other hand, many researchers have adopted an experimental approach to study the effect of flaw geometry on the mechanical response of flawed specimens. Jin et al. (2017) conducted uniaxial compressive tests on single-flawed prismatic specimens to study the effect of flaw inclination angle on *UCS*. Their findings showed *UCS* declined at $\alpha = 15°$, followed by a steady rise at $\alpha = 90°$. Yang et al. (2018) experimentally investigated the impact of flaw inclination angle on the mechanical properties of prismatic sandstone specimens containing one oval flaw. The results suggested that *UCS* declines at $\alpha = 15°$ and rises continuously at $\alpha = 90°$, *E* experiences a virtually similar trend, and the peak strain is marginally influenced as the flaw inclination angle increases. Wang et al. (2020) investigated the effect of flaw inclination angle on the mechanical properties of a rock plate containing a central flaw experimentally. Their results showed that *UCS*, *E*, and peak axial strain grow as the flaw inclination angle rises. Karimi et al. (2021) conducted experimental tests on cylindrical specimens to evaluate the impact of flaw inclination angle, length, and aperture. They reported that *UCS* rises as flaw inclination angle increases from 0° to 75°, while it drops when flaw length increases. Moreover, *UCS* is virtually affected by flaw aperture at low flaw length, whereas with the length increasing, *UCS* is affected marginally and experiences a decline at $\alpha = 45°$.

As for crack initiation and development, many investigators have conducted uniaxial tests on rock-like and natural flawed-rock specimens (Zhang and Wong 2012). Several researchers have adopted experimental methods and reported a typical crack pattern: tensile wing cracks evolving curvilinearly from flaw tips and secondary cracks, that are shear ones, propagating coplanar with the flaw or in the opposite direction of wing cracks (Bobet 2000). Bobet and Einstein (1998b) investigated the Boundary Element Method's application for the crack coalescence simulation. They used the results of uniaxial compressive tests on two-flaw prismatic samples made of gypsum to verify the numerical results. Bobet (2000) proposed a criterion for initiating wing and secondary cracks from existing flaws for specimens subjected to compressive loading. Bobet and Einstein (1998a) studied the crack coalescence and propagation of prismatic samples containing two flaws, either closed or opened under

uniaxial and biaxial compression. They reported two types of cracks, including wing cracks and secondary cracks. Wong et al. (2001b) and Tang et al. (2001a) studied the cracking processes of rock-like materials containing three frictional flaws under axial loading. They indicated that the arrangement and friction of flaws considerably impact how cracks coalesce. Li et al. (2005) investigated crack evolution of prismatic pre-cracked marble specimens subjected to axial compressive loading. They suggested that the type of wing and secondary cracks depend on the existing flaw's orientation and geometry. Wong and Einstein (2006) indicated that the cracking processes of a single flawed prismatic specimen subjected to axial loading are affected by material type, flaw aperture, and inclination. Wong and Einstein (2009) classified the failure pattern of prismatic specimens under axial loading made of molded gypsum and marble containing one flaw into seven types, including three tensile types, three shear types, and mixed tensile-shear one. Zhou et al. (2014) experimentally studied the effect of the arrangement of cracks on cracking processes of prismatic samples containing four flaws subjected to uniaxial compressive load and classified five types of crack, including wing crack, quasi-coplanar secondary crack, oblique secondary crack, out-of-plane tensile crack, and out-of-plane shear crack, and identified ten modes of crack coalescence. Liu et al. (2015) conducted uniaxial compressive experiments on prismatic specimens with two parallel flaws to investigate the impact of flaw geometry on the cracking process, which led to classifying eight crack types and seven crack coalescence patterns.

On the other hand, many researchers have employed numerical analysis to study crack initiation and development. Zhang and Wong (2012) adopted PFC^{2D} and parallel bond models to study crack development under uniaxial compression and reported that single-flawed specimens' crack initiation and failure pattern are noticeably affected by flaw inclination angle. Additionally, crack initiation stress increases as the flaw inclination angle rises, and the first crack emanates in zones with a high tensile stress concentration. Manouchehrian et al. (2014) conducted numerical uniaxial and biaxial simulations using PFC^{2D} to study the impact of flaw inclination angle on crack development of single flawed specimens, which indicated that wing crack initiates nearer to the tips of flaw as flaw inclination angle rises. Additionally, the initiation angle of secondary cracks decreases with the flaw inclination angle, while that for wing crack increases. Jin et al. (2017) investigated the effect of flaw inclination angle on crack initiation and failure mode of rock-like materials with a single flaw under uniaxial compression loading using PFC^{2D}. They suggested that at the tips of flaws with $\alpha \leq 30°$ and $\alpha \geq 45°$ tensile and shear cracks evolve, respectively. In addition, the failure mode of specimens with $\alpha \leq 30°$ is similar, and that for $\alpha = 90°$ resembles that of the intact specimen. Yang et al. (2018) conducted several *UCS* experiments and numerical investigations using PFC^{2D} on sandstone specimens with one oval flaw. The findings revealed that with the increase of flaw inclination angle, the initiation stress rises, and wing tensile crack occurs at the flaw tip. Shen et al. (2021) conducted uniaxial compressive tests and numerical simulations using PFC^{2D} on prismatic single flawed specimens to examine their cracking process. The results revealed that the distance and angle at which cracks emanate from the flaw tips decline as flaw width rises until it is less than 1.0 mm, while these two values remain stable with a further rise of flaw width. Fan et al. (2021) investigated the impact of undulation and inclination angle of prismatic specimens containing folded flaws on their cracking processes using uniaxial compressive tests and numerical simulations utilizing PFC^{2D}. They reported five failure types and that the connection of shear cracks with the flaw results in coalescence. Huang et al. (2022) studied the fracture mechanism of prismatic three-flaw sandstone specimens using uniaxial compressive tests and PFC^{2D} simulations. They recognized three types of cracks tensile, shear, and mixed tensile shear. They also established that with the rise of flaw inclination angle, tensile stress concentrates at flaw tips rather than the middle point of the flaw.

However, strength, deformational behavior, and cracking process of central-flawed cylindrical specimens subjected to axial loading have been extensively investigated neither in the laboratory nor using the three-dimensional Discrete Element Method (DEM). Most works of literature have reported prismatic physical tests and two-dimensional rectangular numerical models.

In this study, a three-dimensional Particle Flow Code (PFC3D) was adopted to numerically analyze the effect of flaw inclination angle, length, and aperture on the specimens' mechanical behavior, micro and macro crack development, and principal stress concentration at flaw tips in single flawed specimens subjected to axial loading. For this purpose, the numerical models were calibrated and verified using extensive experimental test results (Karimi et al. 2021; Asadizadeh et al. 2022), and then an extensive numerical simulation was conducted. Finally, a comprehensive comparison between experimental and numerical results was made.

Experimental program

An extensive experimental investigation was carried out on cylindrical specimens measuring 120 mm in length and 54 mm in diameter made of dental plaster to establish the effect of flaw inclination angle, length, and aperture on the strength and Elastic Modulus of single-flawed specimens (Karimi et al. 2021; Asadizadeh et al. 2022). They

built 64 samples with embedded flaws using a molding technique. The specimens subjected to uniaxial loading were constructed with three flaw lengths, including 13, 26, and 39 mm, and three flaw apertures equal to 1.2, 2.0, and 2.8 mm. For a specific flaw length and flaw aperture, flaw inclination angle, measured from the horizon, ranged from 0° to 75° with an interval of 15°. In this study, specimens' unconfined compressive strength (*UCS*) and failure patterns were measured and examined carefully. A full description of experimental experiments and their results can be found in the published papers (Karimi et al. 2021; Asadizadeh et al. 2022).

Numerical modeling

The rupture of flawed rocks, which are a complicated system of the rock matrix and open or closed flaws, might transpire either within the matrix, along the discontinuities, or in both. PFC^{3D} employs a flat-joint bonded-particle model (FJ-BPM), which can satisfactorily replicate the mechanical response of actual rock samples and the initiation and propagation of cracks (Sun et al. 2019). Stress concentration and crack development around an open flaw can be easily simulated using PFC^{3D} and the flat-joint model.

Flat-joint bonded-particle model

In FJ-BPM, the contact of each two particles or pieces, formed by two notional surfaces rigidly connected to a particle and called faces, is modeled by an interface with a limited size, behaves linearly elastic, and is either bonded or unbonded. The interface is divided into bonded or unbonded elements (Potyondy 2012; Vaziri et al. 2022). The particles of the corresponding flat-jointed materials are called faced grains and are represented by a spherical core and a few skirted faces (Fig. 1).

Each element stores a force and moment determined by Newton's laws of motion, based on which the force and moment of the interface are calculated. A bonded element has linear elastic behavior before the load applied exceeds its bond strength, which leads to its failure, turning it into an unbounded one. By contrast, an unbonded element is frictional and responds linearly elastic, and its slip is governed by a Coulomb limit applied to the shear force. When a

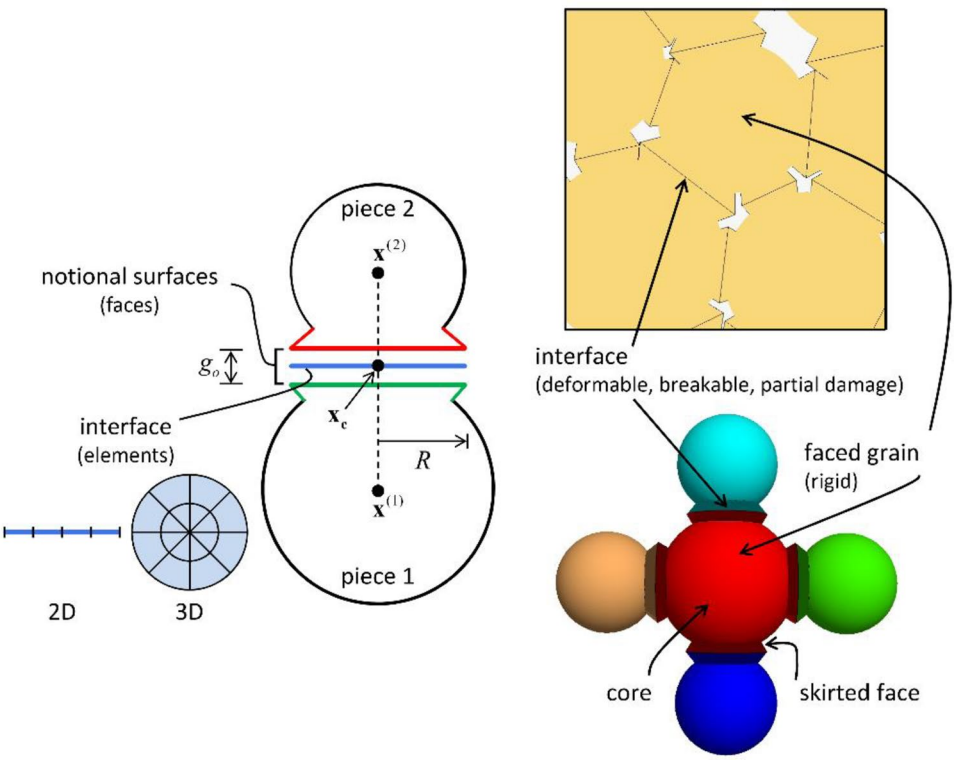

Fig. 1 Flat-joint contact (left); flat-jointed material (right) (Itasca Consulting Group Inc. 2022)

$\mathbf{X}^{(1)}$, $\mathbf{X}^{(2)}$, $\mathbf{X}_c$: location vector of piece 1, piece 2, the interface contact plane, respectively

g_0: the initial contact gap

R: the radius of the interface

bonded element fails and the associated interface is partially damaged, microcracks emerge, and the stress state's redistribution occurs, leading further to the interface breaking. Macroscopic cracks are created while the cracks' growth, expansion, and coalescence occur (Itasca Consulting Group Inc. 2022).

Calibration of flat-jointed BPM

Meso-properties of bonds and particles comprising a PFC model cannot be achieved directly using an experimental method. This means that conducting a trial and error process is necessary using macro-properties calculated from laboratory experiments to obtain these properties used in the subsequent numerical simulations (Bahaaddini et al. 2013b; Itasca Consulting Group Inc. 2022). In this process, mechanical properties of rock, including *UCS*, E, ν, and σ_t, obtained from unconfined compression and indirect tensile tests, are used to calibrate the meso-properties required for a PFC model (Bahaaddini et al. 2013a, b; Itasca Consulting Group Inc. 2022). The first step involves the calibration of *UCS*, E, and ν. For *UCS* tests to be simulated, a PFC model consisting of two approaching walls is created in which the walls at the top and bottom of the samples move towards each other and create compressive loads on the assembly.

The Modulus of elasticity (E), which is a function of the particle elastic modulus (E_c), the elastic Modulus of flat-joint bond ($\overline{E}_c$), the particle normal to shear stiffness ratio ($\frac{k_n}{k_s}$), and the ratio of normal stiffness to shear stiffness of flat-joint bond ($\frac{\bar{k}_n}{\bar{k}_s}$), is the first parameter that is calibrated. Next, Poisson's ratio (ν), depending on $\frac{k_n}{k_s}$, and $\frac{\bar{k}_n}{\bar{k}_s}$, is calibrated in an iterative process. Finally, *UCS*, controlled by the tensile strength and cohesion of flat-joint bonds, is back-calculated (Potyondy 2012; Vaziri et al. 2022). The dimensions of the numerical samples were the same as those of the laboratory specimens mentioned in Sect. 2. The axial stress is monitored using reaction forces on the top, and bottom walls, which move towards each other with a velocity of 0.01 m/s, and axial strain is measured using the displacement of the walls. Lateral displacement was monitored using three pairs of gage balls at both sides of the sample (see red points in Fig. 2). Tensile strength was back analyzed using the results of the Brazilian test. A direct tensile numerical model with the exact dimensions of the laboratory *UCS* sample was generated, and tensile stress was applied to both ends of the model (Vaziri et al. 2022). In PFC^{3D}, stress is measured over a volume rather than in points. Thus, a sphere measuring 40 mm in diameter was created at the model center to record tensile stress (σ_{yy}) over its entire volume. A view of *UCS* and direct tensile strength tests is presented in Fig. 2.

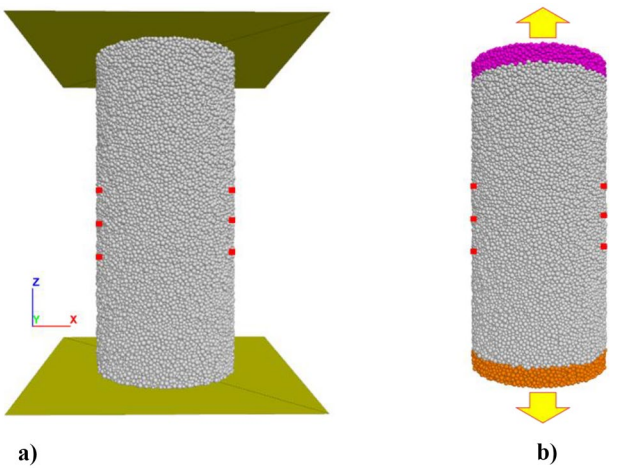

Fig. 2 The generated models for meso-parameters' calibration **a** *UCS* test; **b** direct tensile test

The curves for axial stress versus axial and lateral strains computed based on the numerical and experimental results are shown in Fig. 3. As evident, the numerical and experimental results match each other reasonably.

Moreover, the stress–strain curve for experimental Brazilian disk and numerical indirect tensile tests are presented in Fig. 4. In this paper, compressive strength and deformational behavior of sample are calibrated using UCS test and tensile strength is calibrated using direct tensile test and experimental Brazilian test (Vaziri et al. 2022).

The results obtained from the calibration phase are summarized in Table 1. $R_{\max}$ is the maximum radius of balls in this table, while $R_{\min}$ is their minimum radius. E_c is the ball elastic modulus, and k_n/k_s is the ratio of normal to shear stiffness of ball contacts. $\overline{\lambda}$ is the radius multiplier, and $\overline{E}_c$ is the Elastic Modulus of flat-joint bonds. $\frac{\bar{k}_n}{\bar{k}_s}$ is the ratio of the normal stiffness to the shear stiffness of flat-joint bonds.

Results of uniaxial compression and direct tensile tests are presented in Table 2. There are insignificant differences between the results of the numerical models and laboratory experiments.

Numerical flawed model generation

In this research, a cylindrical specimen is generated using balls with a diameter ranging from 1.2 to 2.0 mm (grey balls in Fig. 5). Since the experimental samples contained flaws with an aperture of 1.2, 2.0, and 2.8 mm, generating numerical models with a clear aperture of 1.2 using the model balls' diameters is difficult. To overcome this hurdle, small balls were used only for the flaw area since using them for the entire model significantly increases

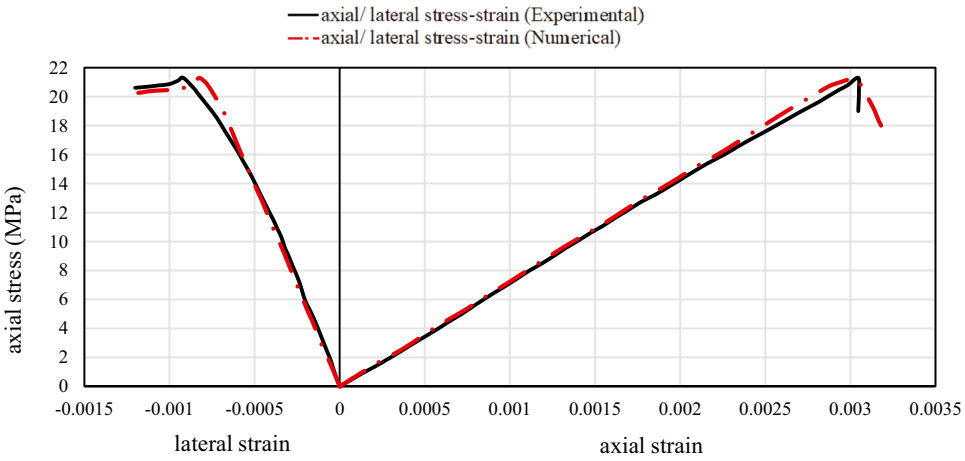

Fig. 3 Stress–strain curves obtained from an experimental and calibrated uniaxial compressive test

the time required for calculations. To accomplish this, the balls in the flaw area are removed over a thickness twice as big as the flaw aperture before packing the sample (Fig. 5a, b). The resulting space is then filled by more petite balls (purple color in Fig. 5c) with diameters ranging from 0.6 to 1.2 mm, and when the packing process finishes, small balls are removed, and the flaw is created with straight surfaces (see Fig. 5d). To measure stress tensor components at flaw tips, two measurement spheres with a diameter equal to 7 mm are installed at flaw tips and on the x–z plane, which is the vertical symmetry plane of the sample (see Fig. 5e). The process is performed and controlled by FISH functions in PFC^{3D} code, and all samples with different flaw aperture were generated using the same procedure. After creating the flaw, the flat-jointed BPM model is assigned to the ball-ball bonds of the numerical model, and now the cylindrical flawed numerical sample is ready to be tested extensively under axial loading.

Effects of flaw geometry on UCS and E

Effect of flaw inclination angle (α) on UCS

Numerical simulations were carried out using PFC^{3D} for various flaw inclination angles (α) ranging between 0° and 90° and for the three flaw lengths ($2a$) and apertures (A). Axial stress and axial strain were recorded during numerical simulations for each numerical model, and *UCS* was calculated. The results of numerical investigations and experimental tests (Karimi et al. 2021; Asadizadeh et al. 2022) are compared in Fig. 6. In this figure, each of the data series represents the effect of flaw inclination angle (α) on *UCS* for a specific flaw length ($2a$) and aperture (A).

When $2a = 13$ mm and $\alpha \leq 30°$ (Fig. 6a), numerical values of *UCS* experience a gradual increase for all the apertures, followed by a noticeable rise at $\alpha = 90°$. *UCS* grows roughly 40% when α rises from 0° to 90°. Turning to the experimental results, they almost agree well with the numerical ones. They experience steady growth as α increases to 75°, which leads to a total change of up to nearly 60%. There is, however, a local decline at $\alpha = 45°$ and $A = 1.2$ and 2.8 mm. This discrepancy could be because of a higher amount of the major principal stress (σ_1) at the flaw tips, which results in lower strength.

Furthermore, for samples with $2a = 26$ mm (Fig. 6b), *UCS* remains virtually unchanged when α rises to 15°, after which *UCS* increases dramatically by 112, 146, and 142%, respectively, as α reaches 90°. However, for $\alpha > 45°$ and $A = 1.2$ mm, the experimental values of *UCS* are virtually higher than the numerical ones. In contrast, the experimental results are slightly lower than the numerical ones over this range of α and $A = 2.0$ and 2.8 mm. Overall, for α ranging from 0° to 75°, experimental values experience a marked rise of 126, 57, and 62%, respectively. The variation of *UCS* in experimental results at each flaw inclination angle may stem from the construction process of the samples, as the numerical results' fluctuation is too low compared with experimental ones.

Finally, when $2a = 39$ mm (Fig. 6c), for $A = 1.2$ mm, numerical results decline gradually at $\alpha = 30°$, followed by a remarkable growth of 260%. However, for $A = 2.0$ and 2.8 mm, *UCS* increases over the entire range of α, experiencing an approximately sixfold increase. On the other hand, the experimental values increase significantly for all three apertures as α ranges from 0° to 75°.

Effect of flaw length (2a) on UCS

Another factor whose effect on *UCS* was investigated is flaw length ($2a$). To illustrate how *UCS* changes as $2a$ increases, for each flaw inclination angle (α), a graph is prepared to show the variation of *UCS* for each aperture both numerically and experimentally (Fig. 7a–f). As evident, both

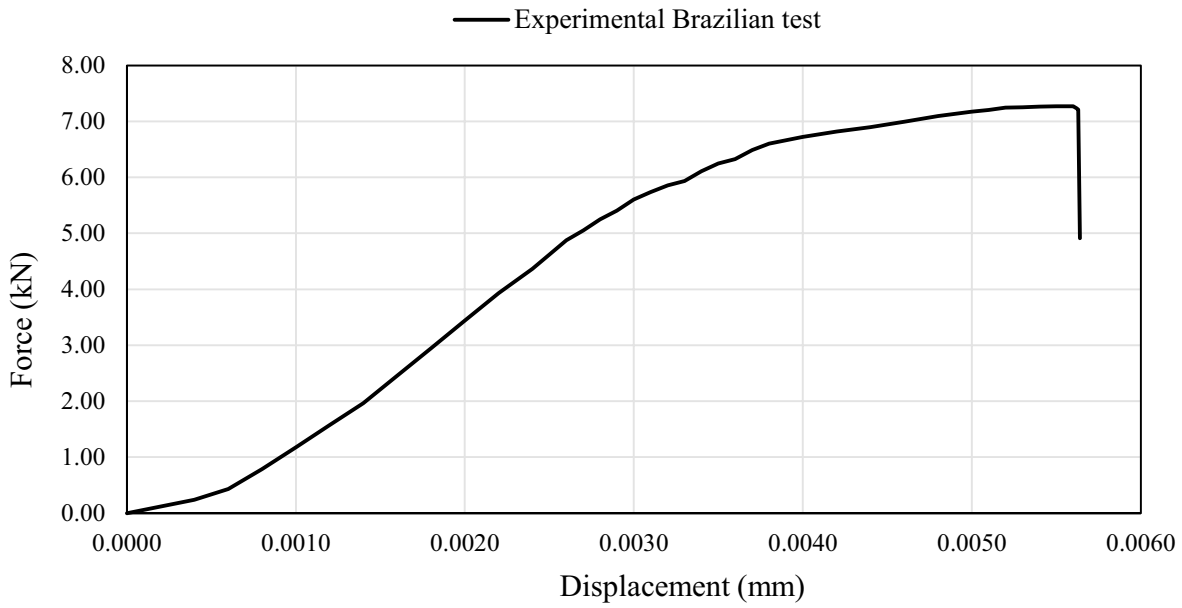

a)

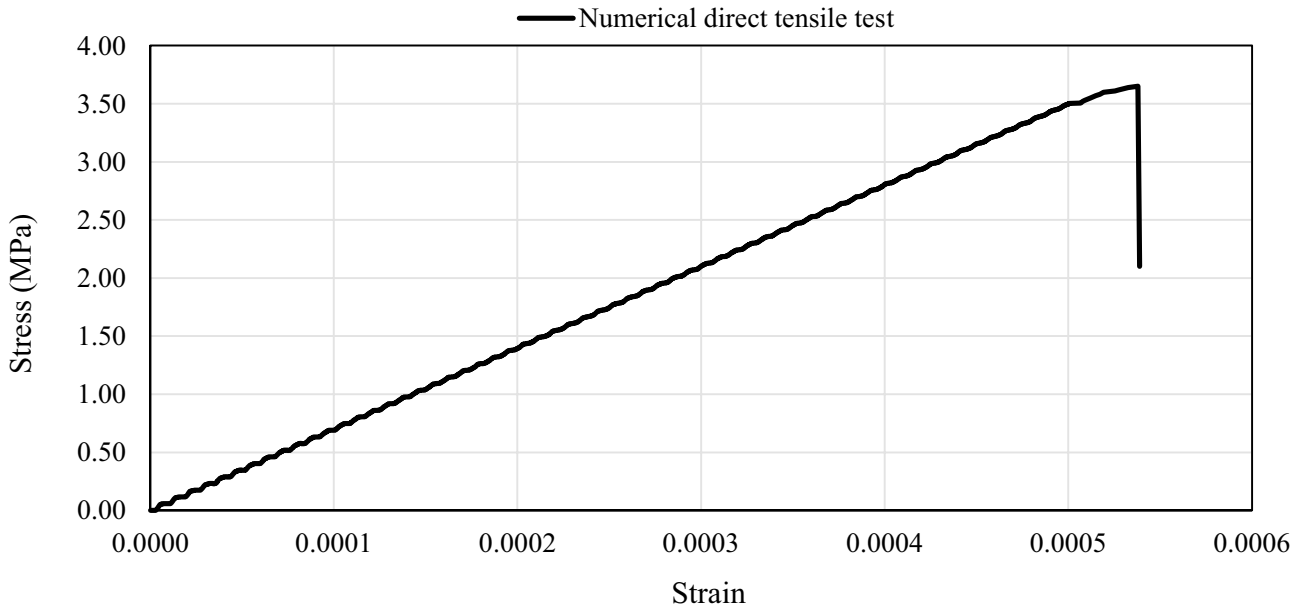

b)

Fig. 4 **a** Force–displacement for experimental Brazilian test. **b** Stress–strain curve for numerical indirect tensile test

numerical and experimental values of *UCS* decline as *2a* rises. When $\alpha \leq 30°$, *2a* has the most significant effect on *UCS*, as with the increase of *2a* from 13 to 39 mm, *UCS* declines by virtually 80% for numerical values and by around 90% for experimental one (Fig. 6a–c). However, the least significant effect of *2a* on *UCS* is observed at $\alpha = 75°$ and 90° (Fig. 7f, g) for experimental and numerical values, respectively, where *UCS* experiences a fall of 44% and 42%,

Table 1 Calibrated meso-parameters of the flat-joint BPM

Ball parameters	Value
Density (kg/m^3)	1200
R_{min}(mm)	0.6
R_{max}/R_{min}	1.66
Friction coefficient	0.50
E_c (GPa)	4
k_n/k_s	2
Friction coefficient, μ	0.5
Falt -joint BPM parameters	Value
$\bar{\lambda}$	1.00
$\bar{E}_c$(GPa)	4
Tensile strenght (MPa)	2.65
Cohision (MPa)	3.75
Friction coefficient	0.577
$\frac{\bar{k}_n}{\bar{k}_s}$	2
Number of elements	4

respectively. It should be noted that the decline of *UCS* with the rise of *2a* steadily decreases as α rises, especially for $\alpha > 30°$. In other words, as α increases, the adverse effect of *2a* on *UCS* weakens.

Effect flaw aperture (A) on UCS

The impact of flaw aperture (*A*) on *UCS* is inferred from Fig. 7a-f. To evaluate this, the values of *UCS* should be considered for a specific flaw inclination angle (α) and flaw length (*2a*). Considering both numerical and experimental results, it is clear from these figures that *UCS* is hardly affected by *A* except for a few experimental cases. These include $\alpha = 45°$, $2a = 13$ mm (Fig. 7d), $\alpha = 60°$, 2a = 26 mm (Fig. 7e), and $\alpha = 75°$, $2a = 26$ mm (Fig. 7f). However, in these cases, the values of *UCS* for $A = 2.0$ and 2.8 mm are approximately equal, and that for $A = 1.2$ mm is greater than those for $A = 2.0$ and 2.8 mm. This means that in those experimental cases, the increase of *A* from 2.0 to 2.8 mm barely affects *UCS*.

Table 2 A comparison between mechanical properties of experimental (Karimi et al. 2021) and calibrated numerical models

Parameter	Experimental	Numerical	Error (%)
E (GPa)	7.00	6.89	1.57
ν	0.27	0.26	3.70
UCS (MPa)	21.30	21.28	0.09
σ_t (MPa)	3.70	3.65	1.35

Effect of flaw inclination angle (α) on E

The modulus of elasticity (*E*) was computed for each numerical model from the axial strain-axial stress curve obtained during numerical simulations. Since this parameter was not measured in the laboratory, a comparison between numerical results and experimental ones is not performed. The numerical results are illustrated in Fig. 8a-c. As can be seen, *E* increases as α rise to 75°, after which it grows at a considerably lower rate at $\alpha = 90°$. While *E* experiences an average growth of 10% for $2a = 13$ (Fig. 8a), it approximately doubles for $2a = 26$ and 39 mm over the entire range of α (Fig. 8b, c). It should be noted that for $2a = 39$ mm, the values of *E* first fall slightly at $\alpha = 15°$ before rising at $\alpha = 90°$.

Effect of flaw length (2a) on E

The impact of flaw length (*2a*) on *E* is shown in Fig. 9a-g. As can be seen, the increase in flaw length exerts a negative effect on *E*. The highest decline (70%) of *E* occurs at $\alpha = 15°$, while at $\alpha = 90°$, *E* falls merely by 2%. It is noteworthy that the decrease observed in the values of *E* falls as α increases. This is noticeable at $\alpha > 30°$, meaning that flaw length remarkably loses its impact on *E* at a higher flaw inclination angle.

Effect of flaw aperture (A) on E

How *E* is affected by flaw aperture (*A*) is deduced from Fig. 9a-f. To assess this effect, *E* values are considered for a certain flaw inclination angle (α) and flaw length (*2a*). As can be seen, *E* is hardly impacted by flaw aperture except for a few cases. These include $\alpha = 0°$, 15°, and $2a = 26$, and $\alpha = 15°$, 30°, and $2a = 39$ mm where *E* experiences a slight fall of up to 25% as *A* varies from 1.2 to 2.8 mm (Fig. 9a–c).

Stress state at flaw tips

Principal stress calculation

The stress state at flaw tips was measured using two measurement spheres, and all the six components of the stress tensor (i.e., σ_{xx}, σ_{yy}, σ_{zz} σ_{xy}, σ_{xz}, σ_{yz}) were calculated at each mechanical step during the model solving process (see Fig. 5e). Meanwhile, principal stresses (i.e., σ_1, σ_2, σ_3) and their orientations (i.e., $\boldsymbol{n}_1$, $\boldsymbol{n}_2$, $\boldsymbol{n}_3$) were calculated by FISH programing language in PFC^{3D} using the measured components of stress tensors after each mechanical step based on tensor transformation rules of continuum mechanics (Mase et al. 1999). The mechanical step in which the major principal stress (σ_1) reaches its maximum was determined when

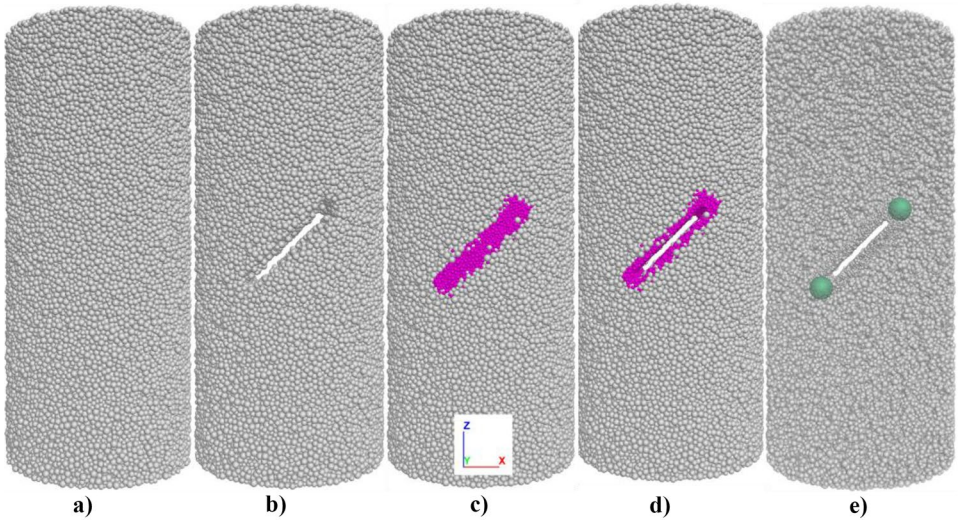

Fig. 5 The process of flaw generation in PFC.[3D] using removing ball techniques; **a** intact sample with coarse balls (gray balls) before packing; **b** removing balls in the flaw area with twice flaw thickness; **c** filling empty area with fine balls (purple balls); **d** removing part of fine balls to create the flaw; **e** installing sphere measurements with diameter 7 mm at both flaw tips (green spheres)

the solving stage ended. The values of the intermediate and minor principal stresses, i.e., σ_2, and σ_3, and their corresponding orientations were calculated, too. It is worth mentioning that the orientation of the maximum of the principal stresses (i.e., σ_1, σ_2, σ_3) at upper and lower flaw tips, which generally occurs on the verge of crack initiation, is mainly $\boldsymbol{n}_1 = \boldsymbol{k}, \boldsymbol{n}_2 = \boldsymbol{i}, \boldsymbol{n}_3 = \boldsymbol{j}$ in all numerical models.

Flaw inclination angle (α)

The effect of α on σ_1 at flaw tips is illustrated in Fig. 10a-c for all three apertures and $2a = 13$, 26, and 39 mm, respectively. At $2a = 13$ mm (Fig. 10a), the values of σ_1 at both upper and lower tips of the flaw are roughly 25 MPa for $\alpha \leq 45°$. For higher values of α, the values of σ_1 at the lower tip of the flaw decreased by nearly one-third at $\alpha = 90°$. Additionally, the values of σ_1 at the upper tip fall at the same rate as those at lower tips at $\alpha = 75°$ before noticeably rising at $\alpha = 90°$. As evident in Fig. 10b, the trend and values of σ_1 for $2a = 26$ mm are virtually like those for $2a = 13$ mm. By contrast, at $2a = 39$ mm (Fig. 10c), the trend is slightly different for $\alpha \leq 45°$. The values of σ_1 at both flaw tips increase steadily, peaking at around 23 MPa at $\alpha = 45°$. When $\alpha > 45°$, the trend and values are virtually the same as those for $2a = 13$ and 26 mm.

One reason for the reduction of σ_1 at $\alpha \leq 45°$ and in models with $2a = 39$ mm, could be the effect of the model boundary. This means that the flaw tips are overly close to the lateral sides of the model. Hence, stress concentration cannot increase at flaw tips because of the impending failure of the area between the flaw tips and the models' lateral sides. However, when $\alpha > 45°$, the distance between the flaw tips and the models' boundary increases, and σ_1 may not be affected by the boundaries. Therefore, the trend at $\alpha > 45°$ is the same for models with $2a = 13$ and 26 mm.

As regards σ_2, Fig. 11a-c show how this stress component is affected by flaw inclination angle for the three flaw lengths and apertures. At $2a = 13$ and 26 mm (Fig. 11a, b), the values of σ_2, at both upper and lower tips, decline considerably from nearly 7 MPa to around 3 MPa at $\alpha = 45°$ and remain at around this value at $\alpha = 60°$ before declining to about 1 MPa at $\alpha = 90°$. It is worth mentioning that the state of this principal stress at the upper flaw tip and $\alpha = 90°$ is tensile and lower than 1 MPa. At $2a = 39$ mm (Fig. 11c), however, the trend is different. The value of σ_2 first increases as α varies from 0° to 30°, followed then by a decline at $\alpha = 60°$. After that, σ_2 rises noticeably at $\alpha = 75°$ before falling considerably at $\alpha = 90°$. Note that at this flaw inclination angle, the state of σ_2 at both flaw tips is tensile, and its values are below 1 MPa. In this case, like σ_1, σ_2 is probably affected by the boundary of the model; however, this effect on σ_2 diminishes at $\alpha \geq 30°$, while this happens at $\alpha \geq 45°$ for $\sigma 1$.

Finally, as evident from Fig. 12, in models with $2a = 13$ and 26 mm (Fig. 12a, b), the minor principal stress (σ_3) at both flaw tips is approximately 2.5 MPa for $\alpha \leq 30°$, before experiencing a marked fall at $\alpha = 75°$, where σ_3 becomes virtually zero. When $\alpha = 90°$ and $2a = 13$ mm, this stress is compressive at the lower tip and tensile at the upper tip with almost the same values. In contrast, for $2a = 26$ mm and this flaw inclination angle, σ_3 is tensile at both flaw tips, and its magnitude is below 1.5 MPa. However, when $2a = 39$ mm (Fig. 12c), the values of σ_3 at upper and lower tips rises steadily as α ranges from 0° to 45°, before experiencing a trend like those for $2a = 26$ mm over the remaining range of α.

It seems σ_3 is not too sensitive to the interaction of the flaw tip and the model's boundary. At all $2a$, σ_3 is maximum around $\alpha = 60°$.

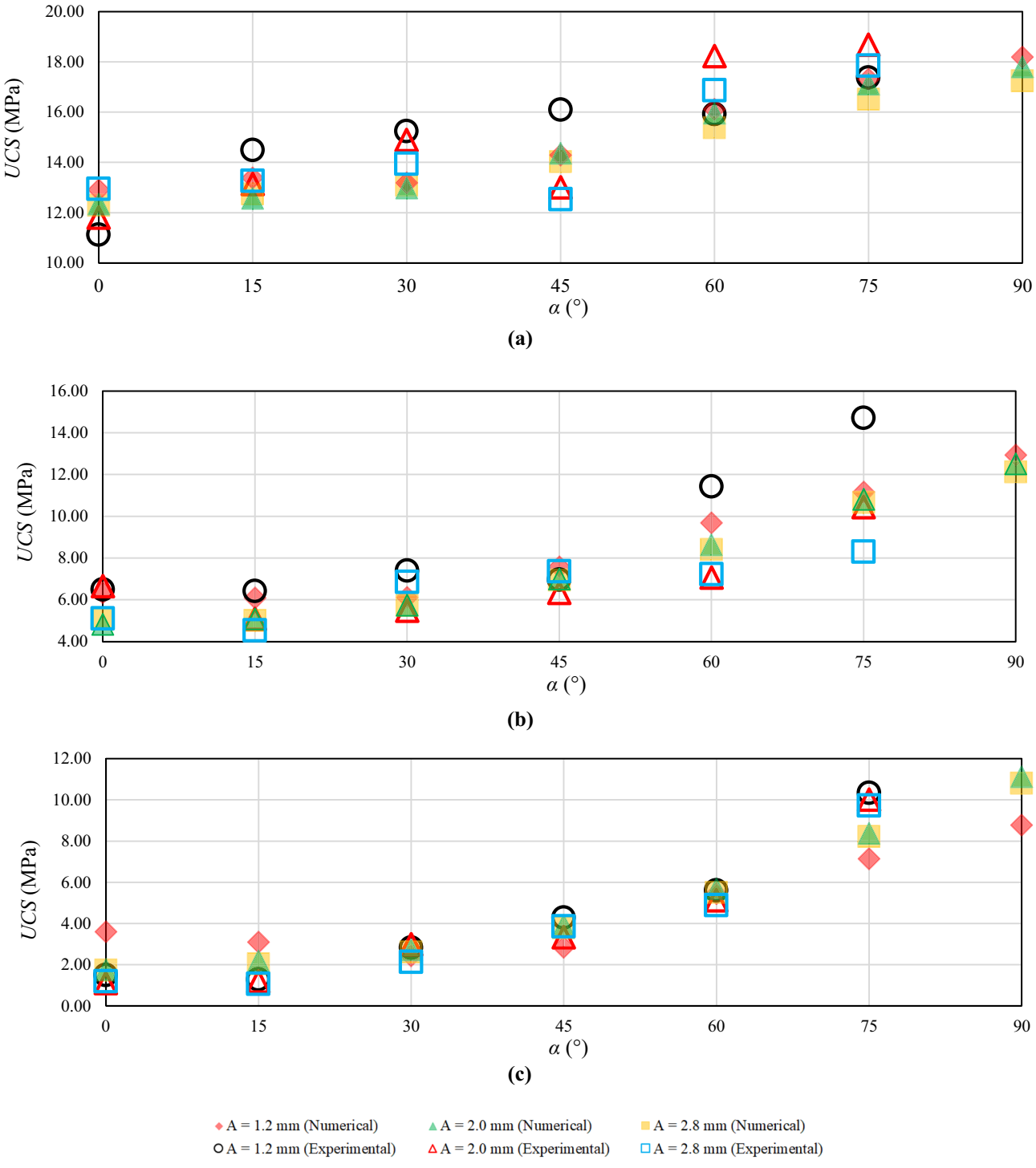

Fig. 6 Effect of flaw inclination on the *UCS* of experimental (Karimi et al. 2021) and numerical models, **a** $2a = 13$ mm, **b** $2a = 26$ mm, **c** $2a = 39$ mm

Flaw length (2a)

When flaw length alters, the values of the three principal stresses might vary subsequently at flaw tips. The following figures evaluate this impact on σ_1, σ_2, and σ_3 at various flaw inclination angles and apertures (Figs. 13, 14, 15, respectively).

It can be seen from Fig. 13 that three different patterns are identifiable. As $2a$ rises, σ_1 generally falls when $\alpha \leq 60°$ (Fig. 13a–e). The next trend is observed for $\alpha = 75°$,

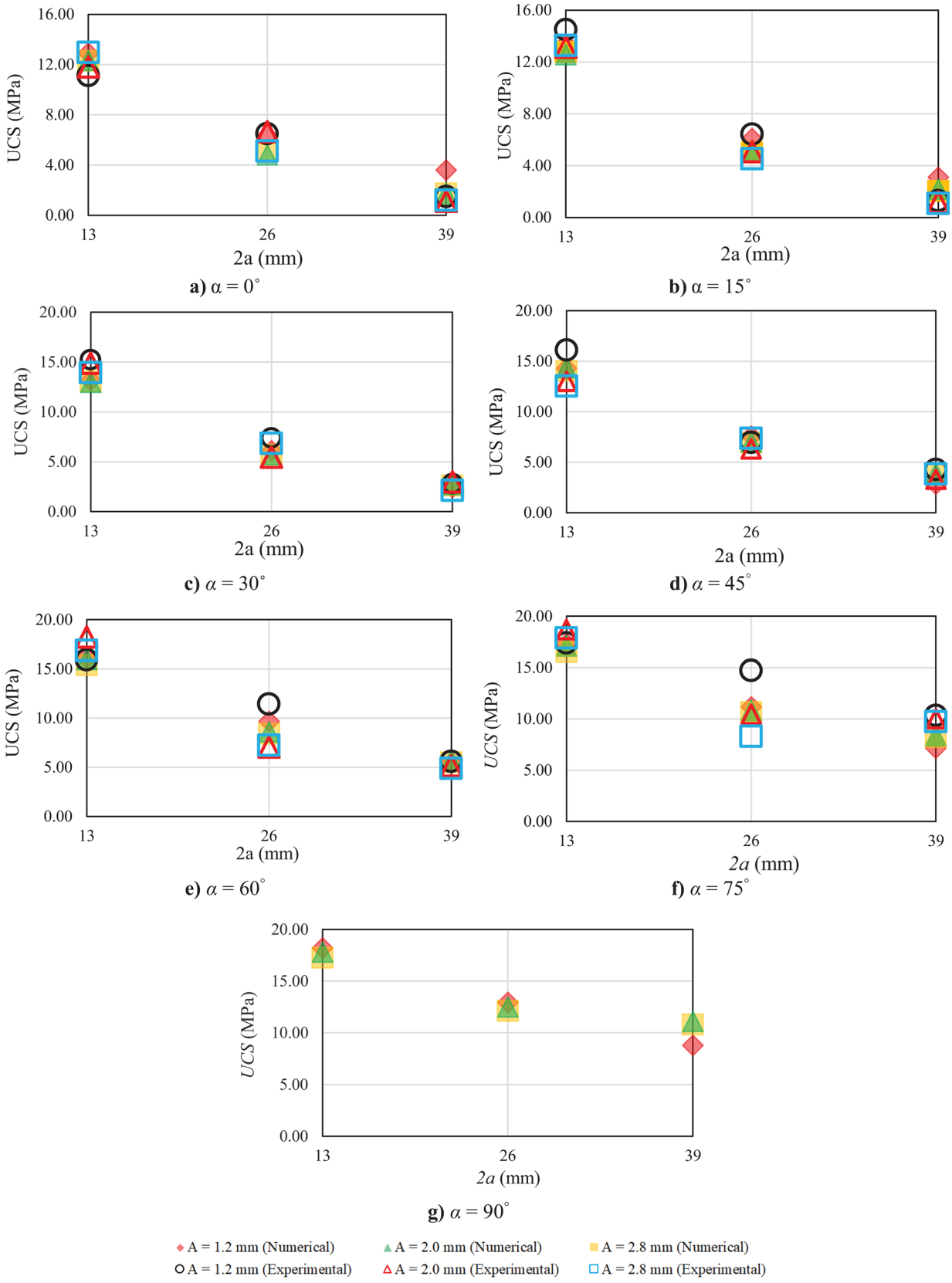

Fig. 7 Effect of flaw length (*2a*) on the *UCS* of experimental (Karimi et al. 2021) and numerical models

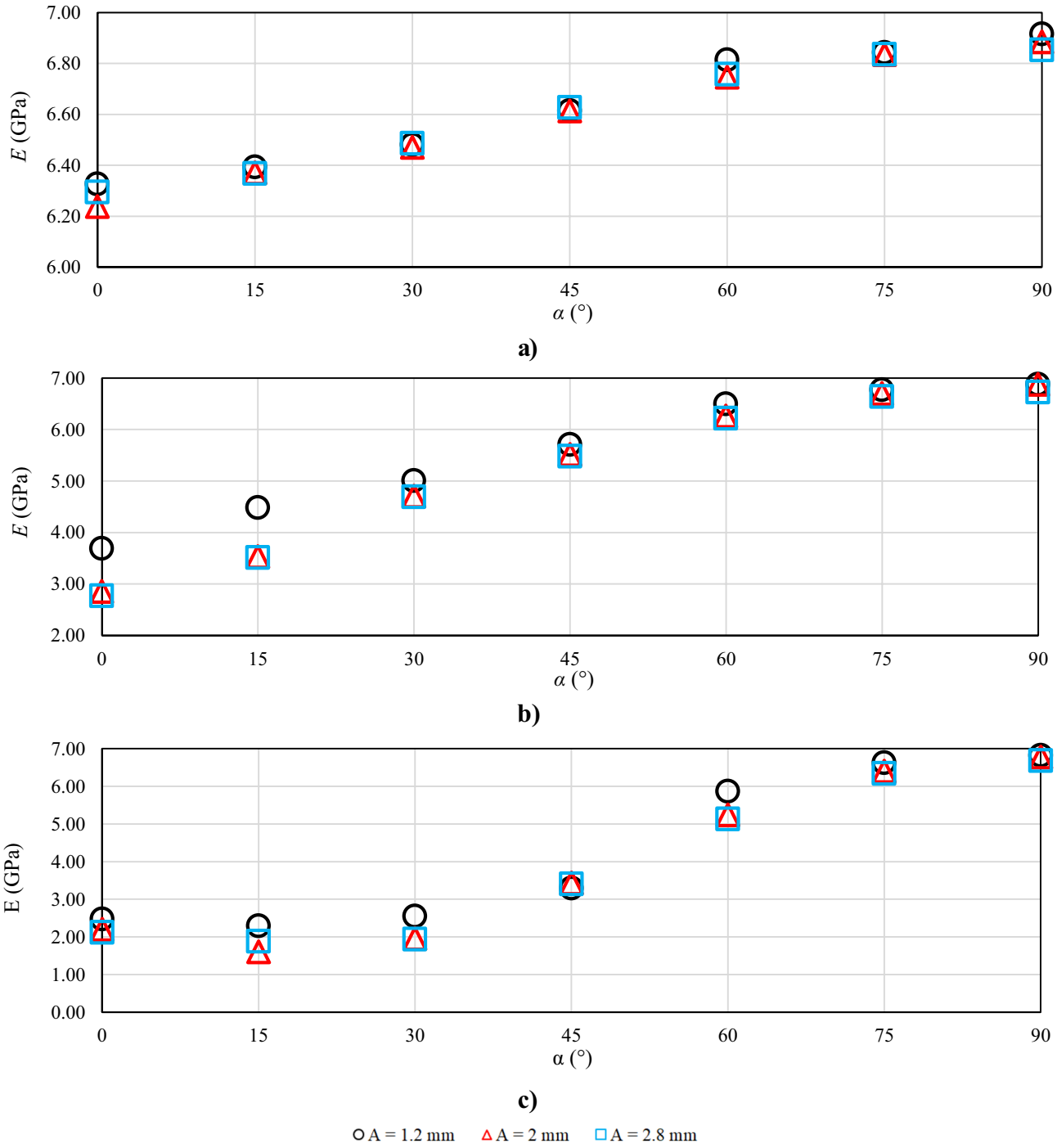

Fig. 8 Effect of flaw inclination angle (α) on E, **a** $2a = 13$ mm, **b** $2a = 26$ mm, **c** $2a = 39$ mm

where with $2a$ increasing, the values of σ_1 decrease first at 2a = 26 mm before increasing at 2a = 39 (Fig. 13f). In the third pattern, at $\alpha = 90°$, the values of $\sigma 1$ at flaw tips remain roughly stable.

Regarding the impact of $2a$ on σ_2, this stress component rises at $2a = 26$ mm followed by decline at $2a = 39$ mm when $\alpha \leq 75°$ (Fig. 14a–g). For $\alpha = 90°$, the values of σ_2 remain almost unchanged. Although the state of σ_2 at $2a = 39$ and the lower tip is tensile, its magnitude is virtually equal to those in other flaw lengths (Fig. 14f).

Finally, the impact of $2a$ on σ_3 is shown in Fig. 15 for both upper and lower flaw tips. This principal stress component

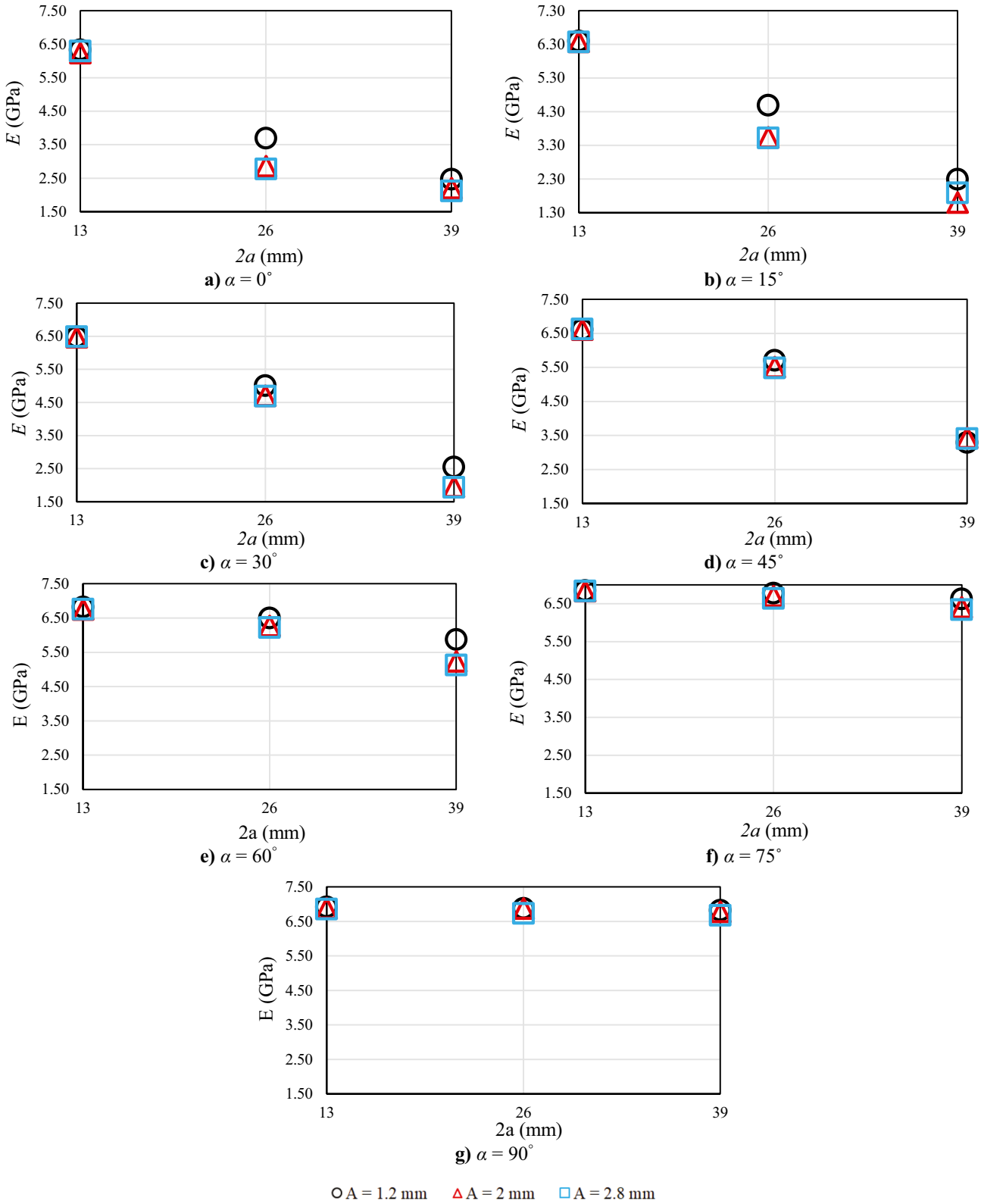

Fig. 9 Effect of flaw length ($2a$) on E

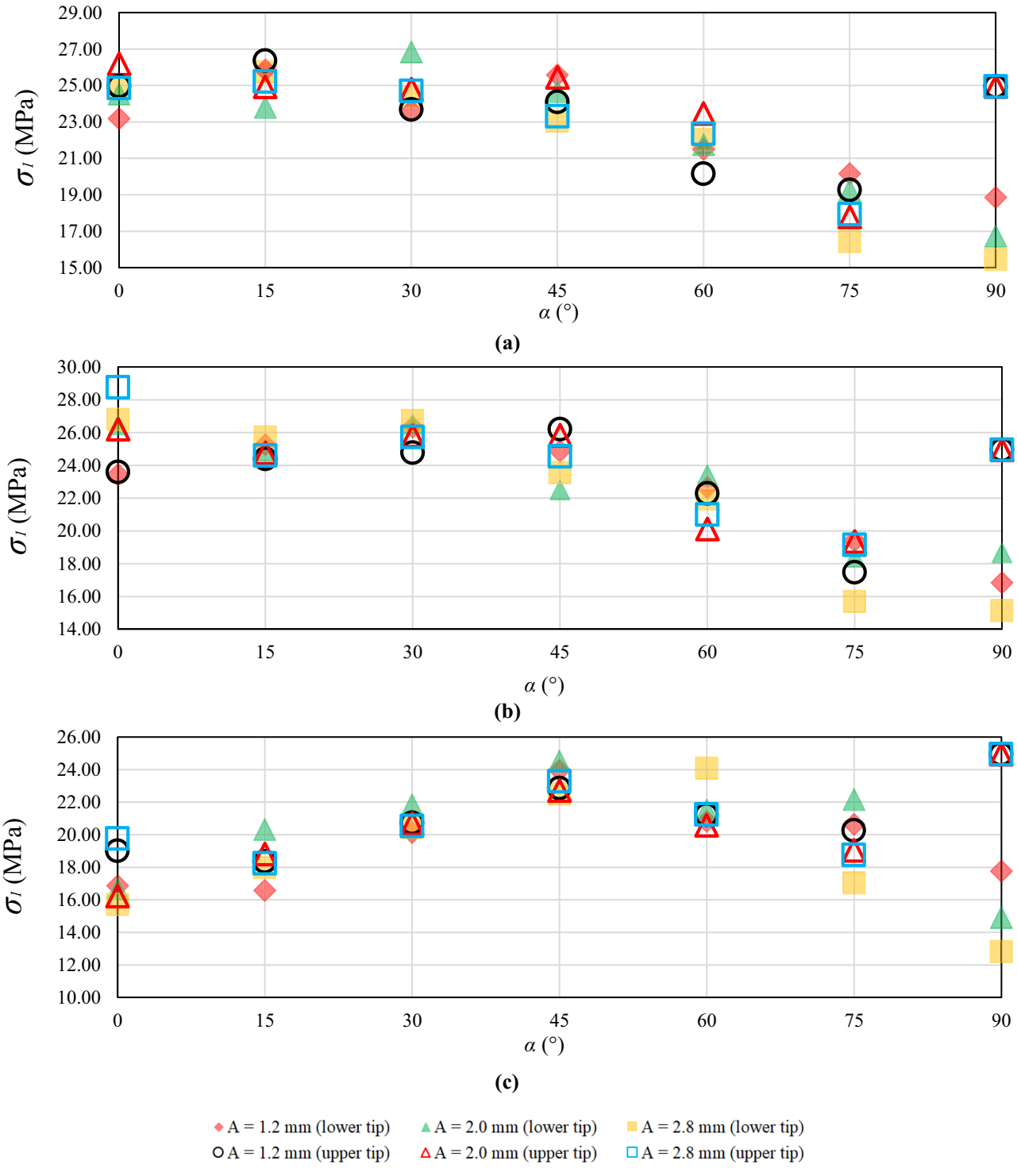

Fig. 10 Effect of flaw inclination angle (α) on major principal stress (σ_1), **a** $2a = 13$ mm, **b** $2a = 26$ mm, **c** $2a = 39$ mm

generally increases and then declines as $2a$ varies from 13 to 39 mm and when $\alpha \leq 45°$. For $\alpha = 60°$, two distinct trends are observed for the values of σ_3 at the lower and upper tips. The σ_3 is nearly 0.5 MPa at the former tip while generally increasing at the latter tip. In addition, when $\alpha = 75°$, σ_3 tends to rise gradually over the range of $2a$. At $\alpha = 90°$, σ_3 hardly changes and remains lower than 1.5 MPa at both lower and upper tips.

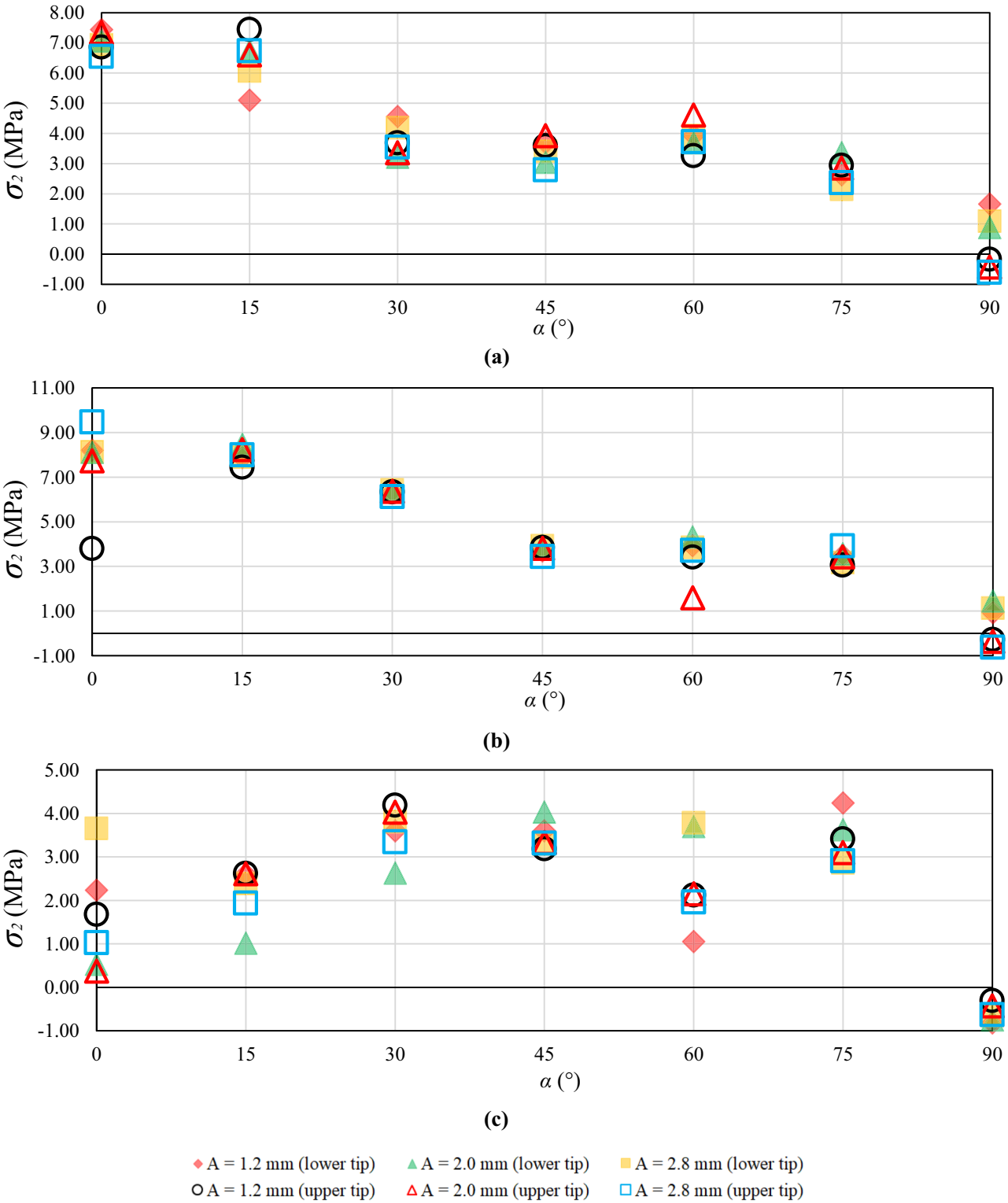

Fig. 11 Effect of flaw inclination angle (α) on intermediate principal stress (σ_I), **a** $2a = 13$ mm, **b** $2a = 26$ mm, **c** $2a = 39$ mm

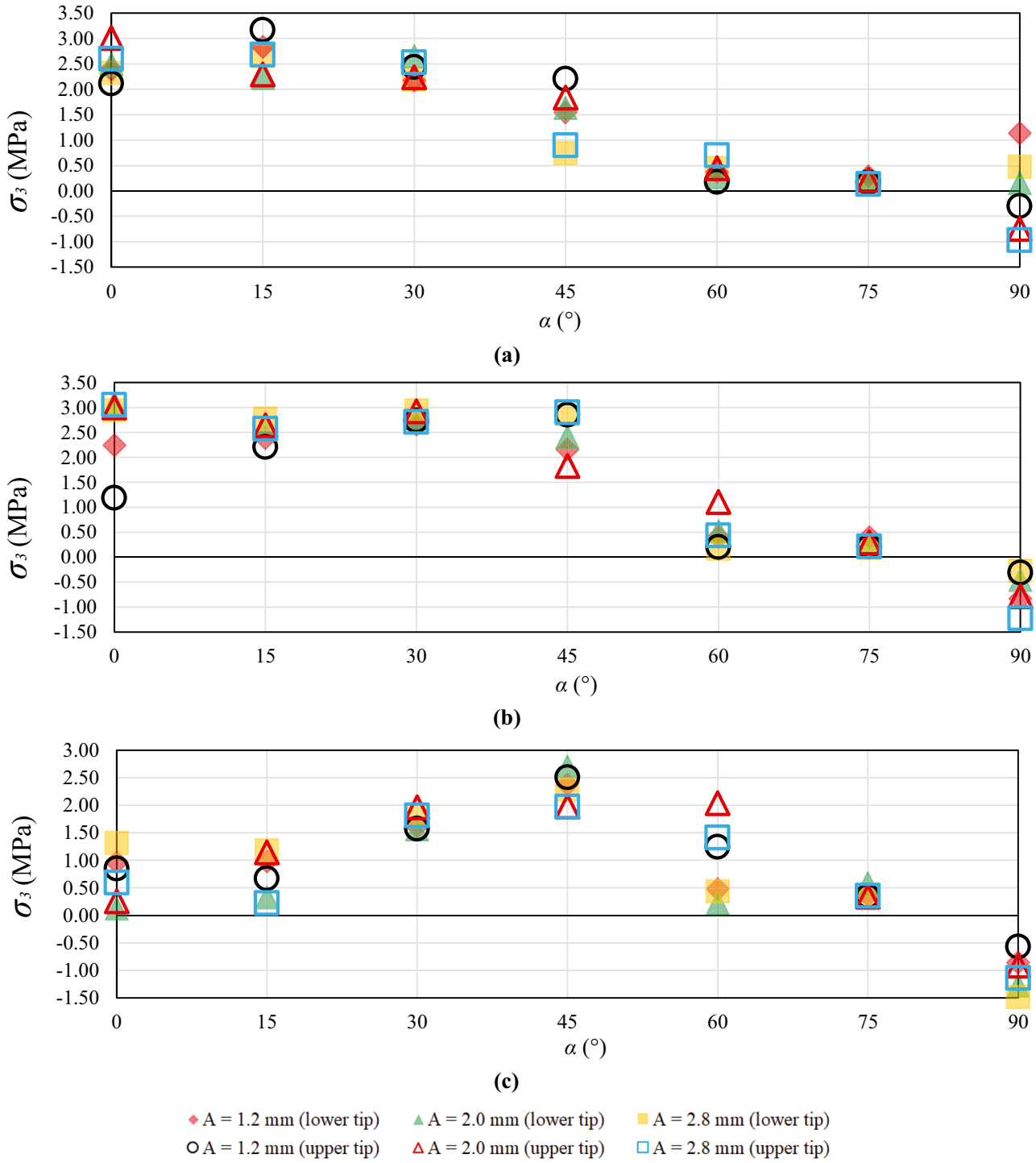

Fig. 12 Effect of flaw inclination angle (α) on the minor principal stress (σ_1), **a** $2a = 13$ mm, **b** $2a = 26$ mm, **c** $2a = 39$ mm

Flaw aperture (A)

The last flaw geometry parameter, the effect of which on the principal stresses is investigated, is flaw aperture (A). To evaluate this effect, the values of the principal stresses at a certain flaw inclination angle and flaw length are considered in Figs. 13, 14 and 15 for σ_1, σ_2, and σ_3, respectively.

As shown in Fig. 13, the values of σ_1, at both upper and lower tips, are nearly the same as A varies, meaning that A barely impacts σ_1. There are, however, a few exceptions. For

the upper tip's values, the most significant differences are observed at $\alpha = 0°$ and $2a = 26$ and 39 mm (Fig. 13a), where the increase in A results in differences of up to 20% in σ_1. Moreover, for the lower tip's values, the increase of A from 2.0 to 2.8 mm affects the values of σ_1 over the range of $2a$ at $\alpha = 75°$ (Fig. 13f). They are also affected when A rises from 1.2 to 2.0 mm at samples with $\alpha = 90°$ and $2a = 39$ mm (Fig. 13g). The difference between measured σ_1 at the upper and lower crack tip when $\alpha = 90°$ may happen due to the impending failure of the lower flaw tip, resulting in lower σ_1 at the lower flaw tip.

As regards σ_2, Fig. 14 reveals that this principal stress component is almost not affected by A, other than in a few models. These include $\alpha = 0°$ and $2a = 26$ mm, $\alpha = 45°$ and $2a = 13$ mm, and $\alpha = 60°$ and $2a = 26$ mm for the upper tip's values (Fig. 14a-d, respectively), and $\alpha = 0°$ and $2a = 39$ mm, $\alpha = 60°$ and $2a = 39$ mm, and $\alpha = 90°$ and $2a = 13$ mm for the lower tip's values (Fig. 14d). In these specimens, the change to A results in the variation of σ_2.

Finally, it can be inferred from Fig. 15 that A impacts σ_3 more noticeably and in more samples compared to σ_1 and σ_2. This impact is more significant for $\alpha = 0°$ and $2a = 26$ mm, $\alpha = 45°$ and $2a = 13$ and 26 mm, $\alpha = 60°$ and $2a = 26$ and 39 mm, $\alpha = 90°$ and $2a = 13$ and 26 mm at upper tip (Fig. 15a, d, e and g, respectively), and $\alpha = 0°$ and $2a = 26$ and 39 mm, $\alpha = 75°$ and $2a = 26$ and 39 mm, and $\alpha = 90°$ and $2a = 13$ mm at lower tip (Fig. 15a, f, g, respectively).

Crack development pattern

The cracking process of flawed samples was investigated during numerical simulations using PFC^{3D}. In this research, crack development was monitored as the axial load increased. Cracks are classified into tensile and shear ones and visualized by yellow and red colors. All the macro cracks were classified based on (Wong and Einstein 2009) classification system.

Flaw with 2a = 13 mm

When $2a$ is 13 mm, three sample groups with $A = 1.2$, 2.0, and 2.8 mm with different α ranging from 0° to 75° by 15° intervals were tested experimentally and numerically. Moreover, during numerical simulations, samples with α equal to 90° were tested, too. The crack initiation pattern of the experimental and numerical specimens is presented in Figs. 16, 17, and 18. As shown in these figures, at all three aperture, when $\alpha = 0°$, tensile cracks of type 3 (Wong and Einstein 2009) initiate, which are distinguishable at the meso-level (yellow ones) at both the upper and lower side of the flaw in the numerical and experimental models. However, as axial stress increases in numerical models, other micro shear cracks (red ones) initiate at both flaw tips.

As for numerical models, tensile cracks of type 3 develop more by increasing A. However, this is not the case in experimental models, in which tensile cracks initiate at the flaw tip on one side of the flaw and initiate from the middle of the flaw on the other flaw side (see Figs. 16a, 17a, 18a). As α rises to 15° and 30° tensile cracks of type 1 initiate form both flaw tips in numerical models at all three apertures (see Figs. 16b, c, 17b, c, 18b, c). Furthermore, type 3 tensile cracks initiate from flaw tip after the development of tensile crack of type 1. As for experimental models, at $\alpha = 15°$, this type of crack mainly initiates at either of the flaw tips; however, at $\alpha = 30°$, tensile cracks of type 1 clearly initiate and develop at both flaw tips. In addition, all numerical models at $\alpha = 45°$, 60°, and 75° have the same crack development pattern, in which mixed mode cracks initiate in shear and continue in tension (see Figs. 16d-f, 17d-f, 18d-f). However, both tensile cracks of type 3 and mixed mode are recognized in experimental specimens.

Finally, at $\alpha = 90°$, numerical simulations show conjugate shear cracks at both tips of the flaws. This pattern is observed for all numerical models with different values of A and $2a$ (from Figs. 16–24; see the figures (g)). However, due to the scope of experimental tests, no test was conducted on a sample with $\alpha = 90°$, and more studies need to be conducted.

Flaw with 2a = 26 mm

As for $2a = 26$ mm, the effect of α on the crack initiation pattern of specimens with the three values of A is presented in Figs. 19, 20 and 21 for both experimental and numerical models. At $\alpha = 0°$ in the numerical models, micro tensile cracks (yellow ones) initiate from the upper and lower side of the flaws at all the values of A (see Figs. 19a, 20a, and 21a). These propagate in the same direction as the axial load (Wong and Einstein 2009). As axial stress increases, micro shear cracks initiate at the tips of the flaws. However, in experimental models with $A = 1.2$ and 2.8 mm, tensile cracks of type 1 emerge at the same flaw tip and develop opposite in the vertical direction (see Figs. 19a, 21a). Moreover, in samples with $A = 2.0$ mm, the same pattern develops at just the upper side of the flaw. In contrast, on the other side, the tensile crack emanates from approximately the middle of the flaw, nearer to the left flaw tip, which is the same as that for numerical models (see Fig. 20a).

As α rises to 15°, 30°, 45°, and 60°, tensile cracks of type 1 initiate at both flaw tips in numerical and experimental models (Wong and Einstein 2009). In all these models, the crack initiation pattern is the same. Micro tensile cracks (the yellow one in numerical models) initiate and propagate at

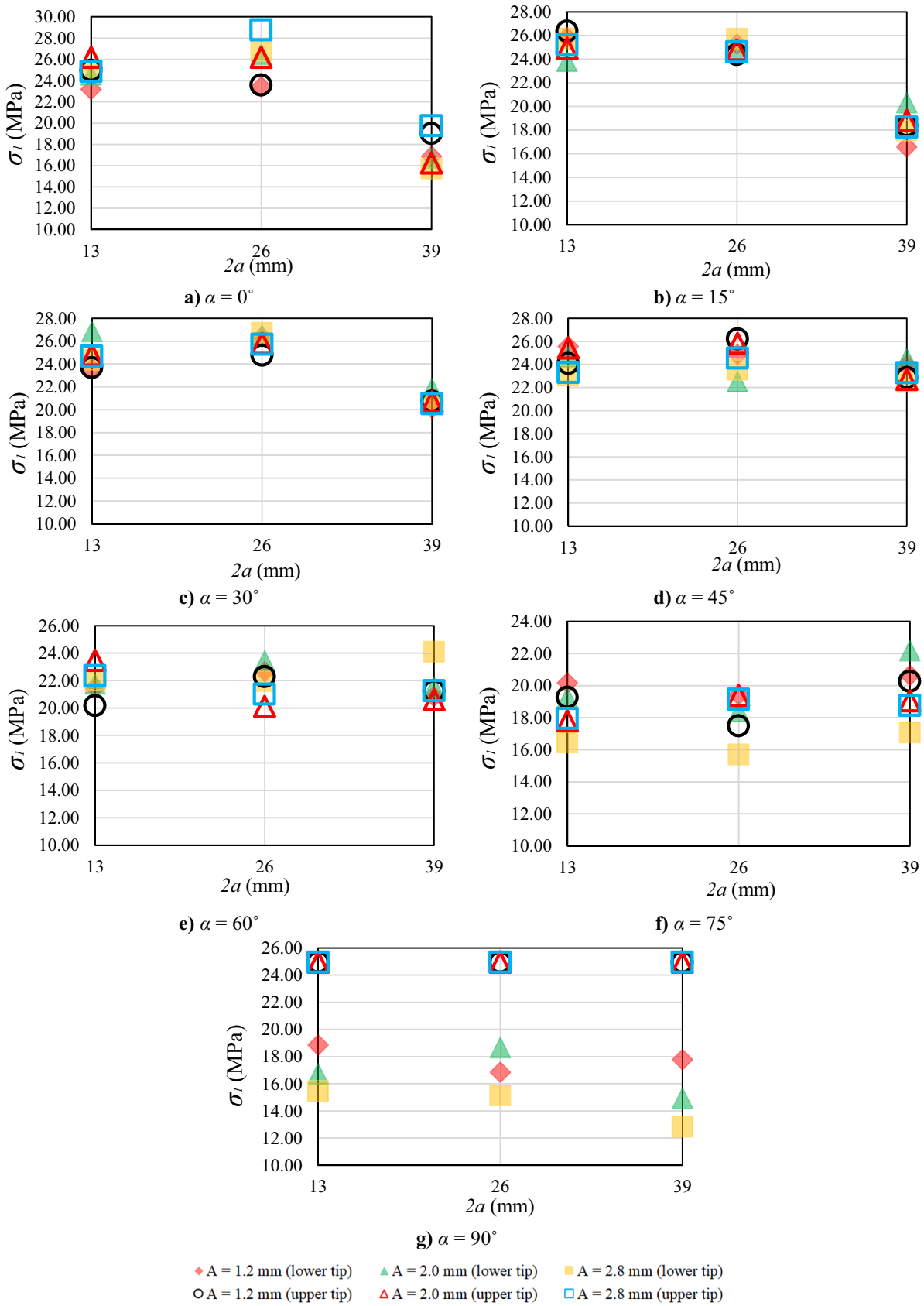

Fig. 13 Effect of flaw length ($2a$) on the major principal stress (σ_1)

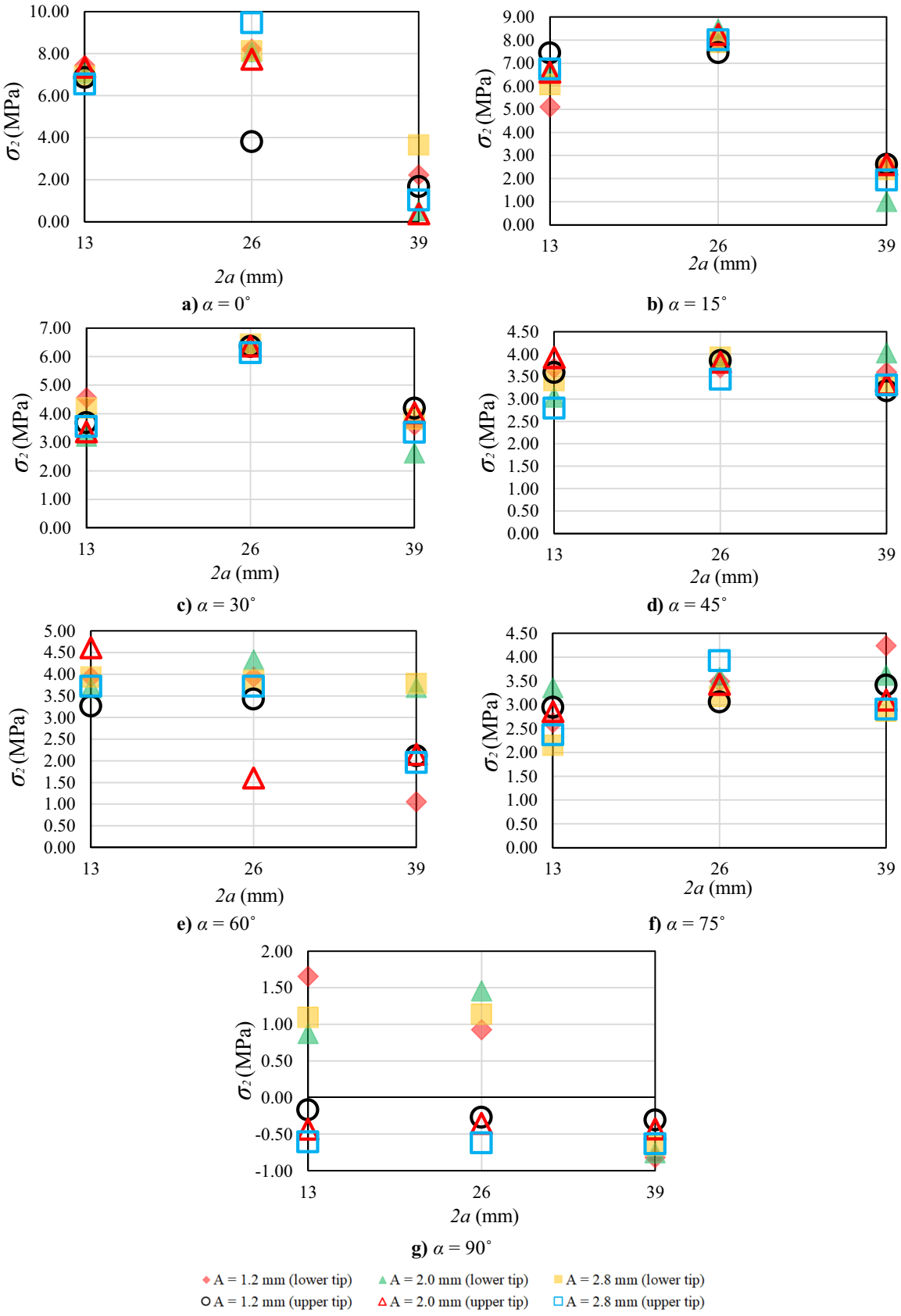

Fig. 14 Effect of flaw length ($2a$) on the intermediate principal stress (σ_2)

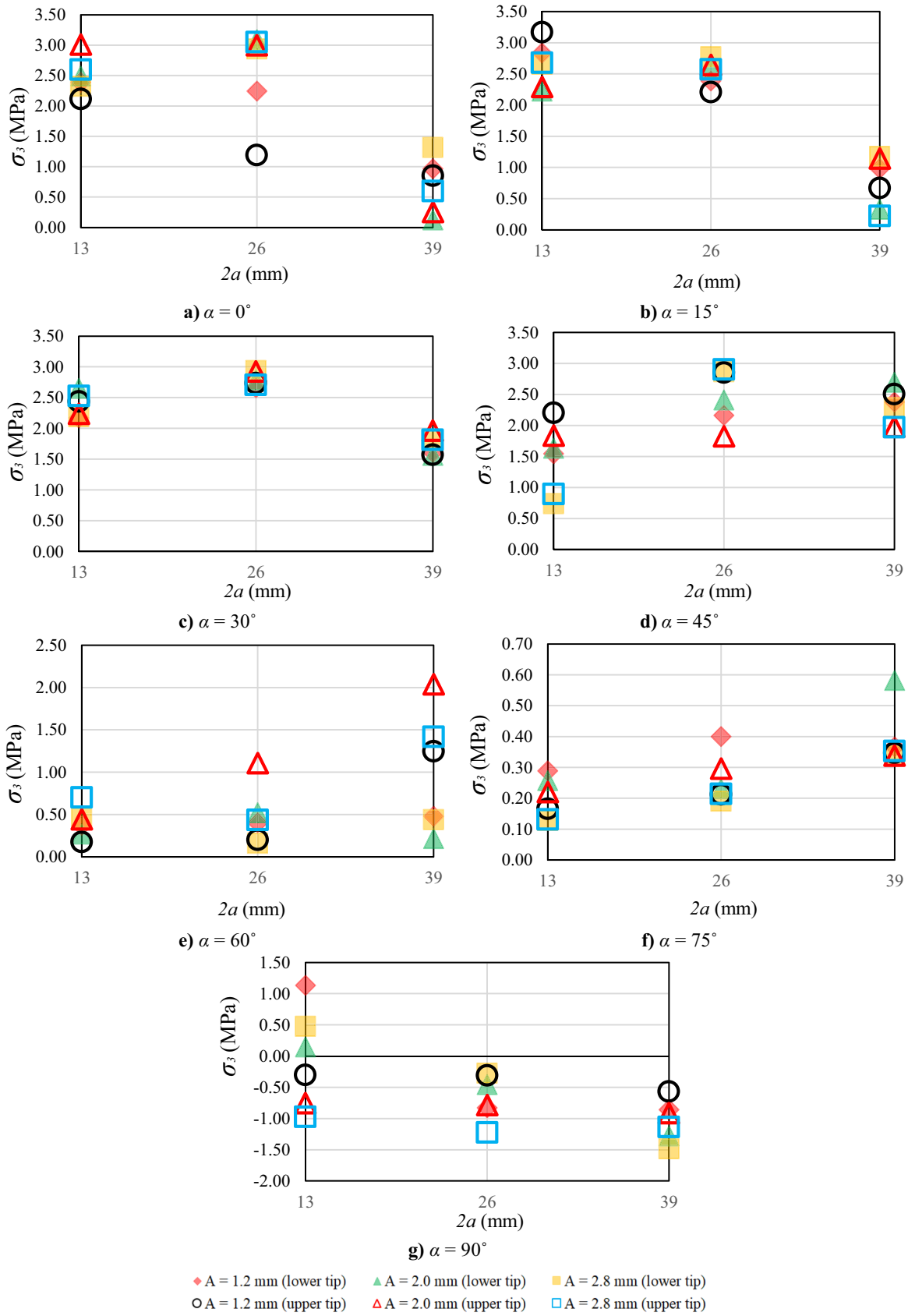

Fig. 15 Effect of flaw length ($2a$) on the minor principal stress (σ_3)

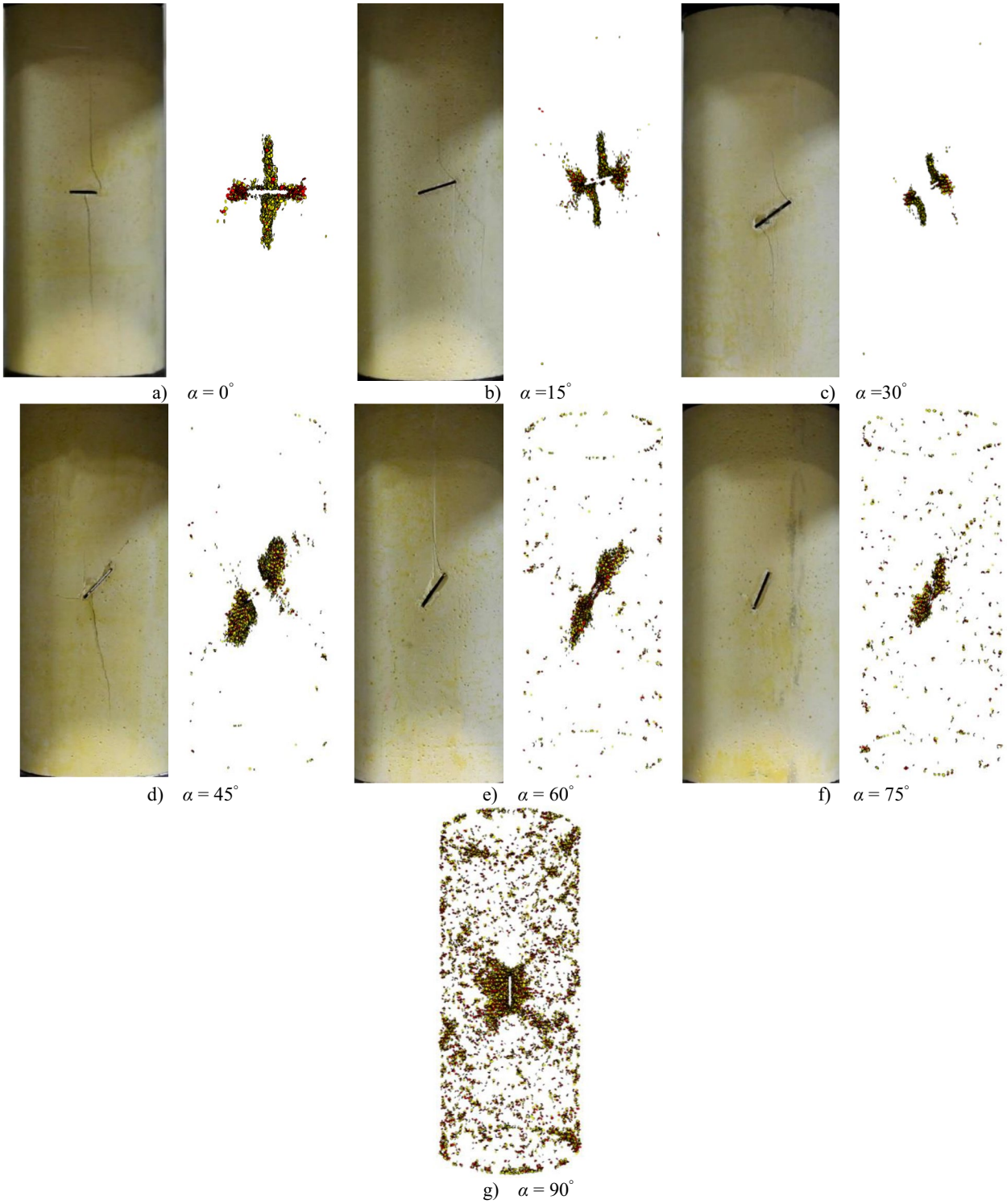

Fig. 16 The effect of flaw inclination angle on crack initiation pattern for specimens with $A = 1.2$ mm and $2a = 13$ mm

both flaw tips and grow parallel to the direction of the axial stress (see Figs. 19b-e, 20b-e, 21b-e).

When $\alpha = 75°$, tensile crack of type 3 (Wong and Einstein 2009) emerges at flaw tips and propagates parallel to the axial load's direction. This pattern is visible in both numerical and experimental models (see Figs. 19f, 20f, 21f). As mentioned for samples with $2a = 13$ mm, the crack initiation pattern for numerical models with $\alpha = 90°$ are the same at different values of A, in which conjugate tensile cracks initiate at flaw tips and propagate towards sample boundaries.

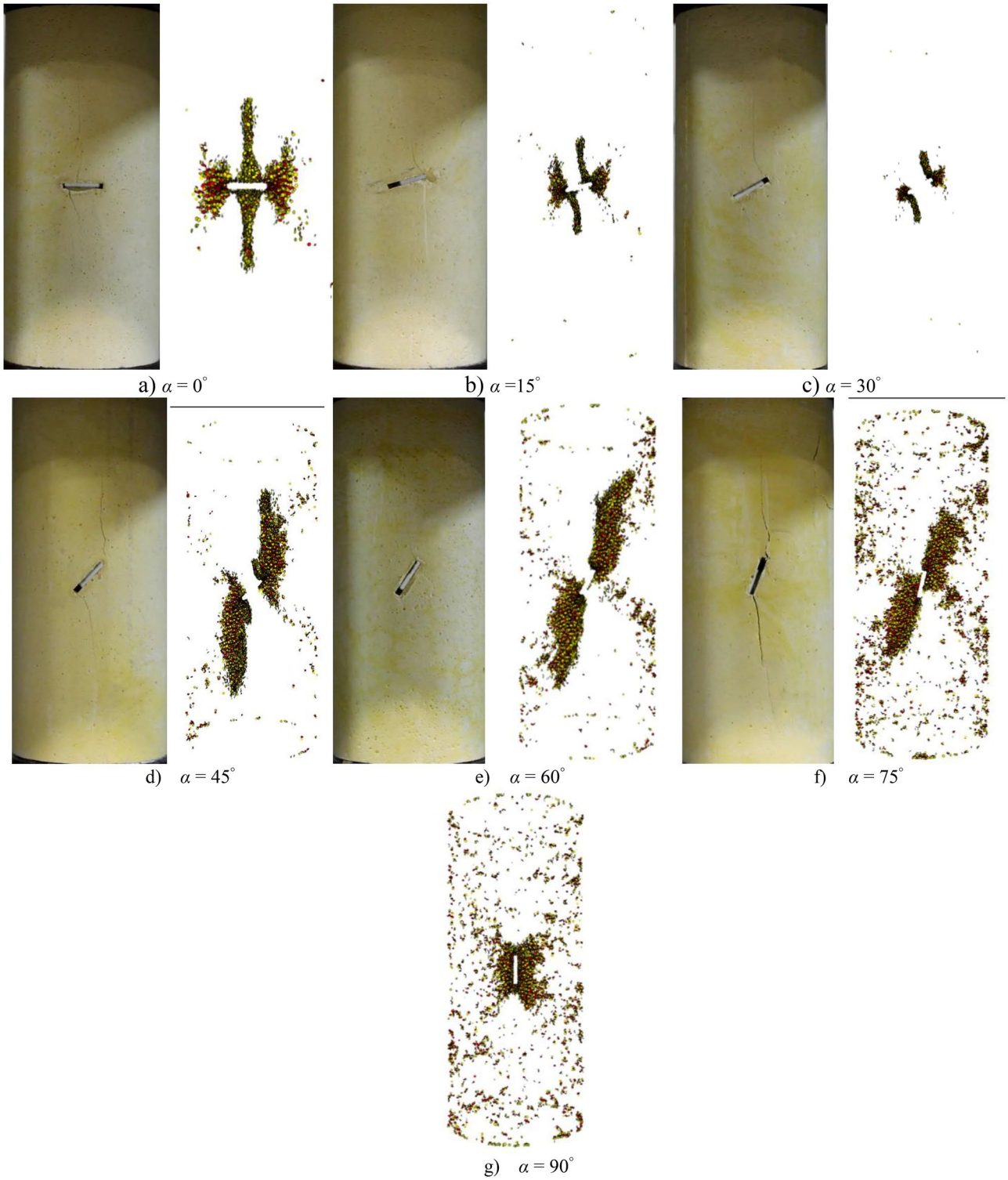

Fig. 17 The effect of flaw inclination angle on crack initiation pattern for specimens with $A = 2.0$ mm and $2a = 13$ mm

Flaw with 2a = 39 mm

When $2a$ is 39 mm, at $\alpha = 0°$, tensile cracks of type 1 initiate at flaw tips, and numerical and experimental crack initiation patterns show some discrepancies. When $A = 1.2$ and 2.0 mm, in numerical models, two identical cracks form on one of the flaw tips while the cracks on the other flaw tip do not propagate (see Figs. 22a, 23a). However, when

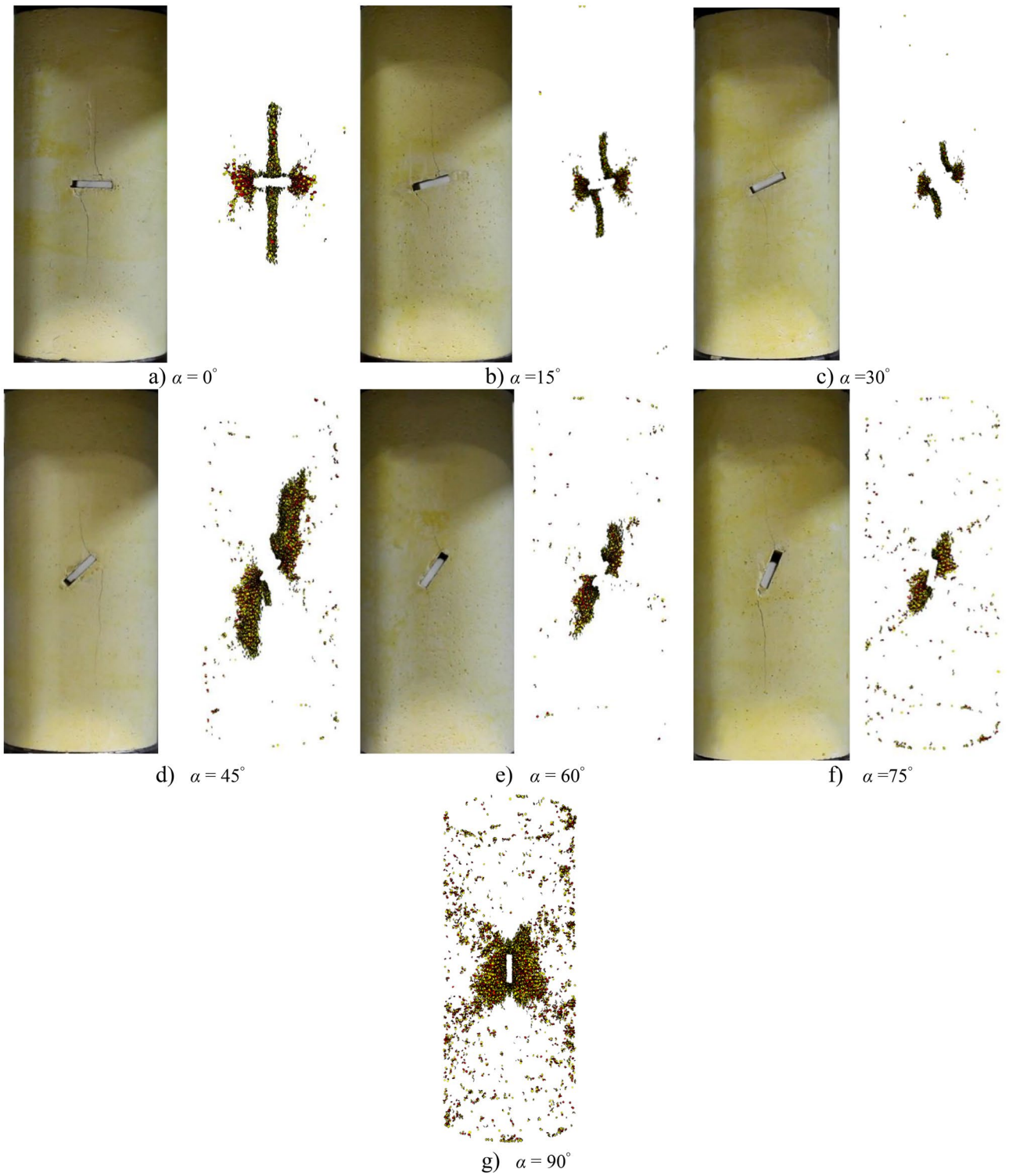

Fig. 18 The effect of flaw inclination angle on crack initiation pattern for specimens with $A = 2.8$ mm and $2a = 13$ mm

$A = 2.8$ mm, two pairs of tensile cracks of type 1 emanate from both flaw tips (see Fig. 24a). On the other hand, in experimental specimens, when $A = 1.2$ and 2.8 mm, a typical tensile crack of type 1 emerges and develops at each flaw tip, whereas when $A = 2.0$ mm, one tensile crack grows at the left flaw tip.

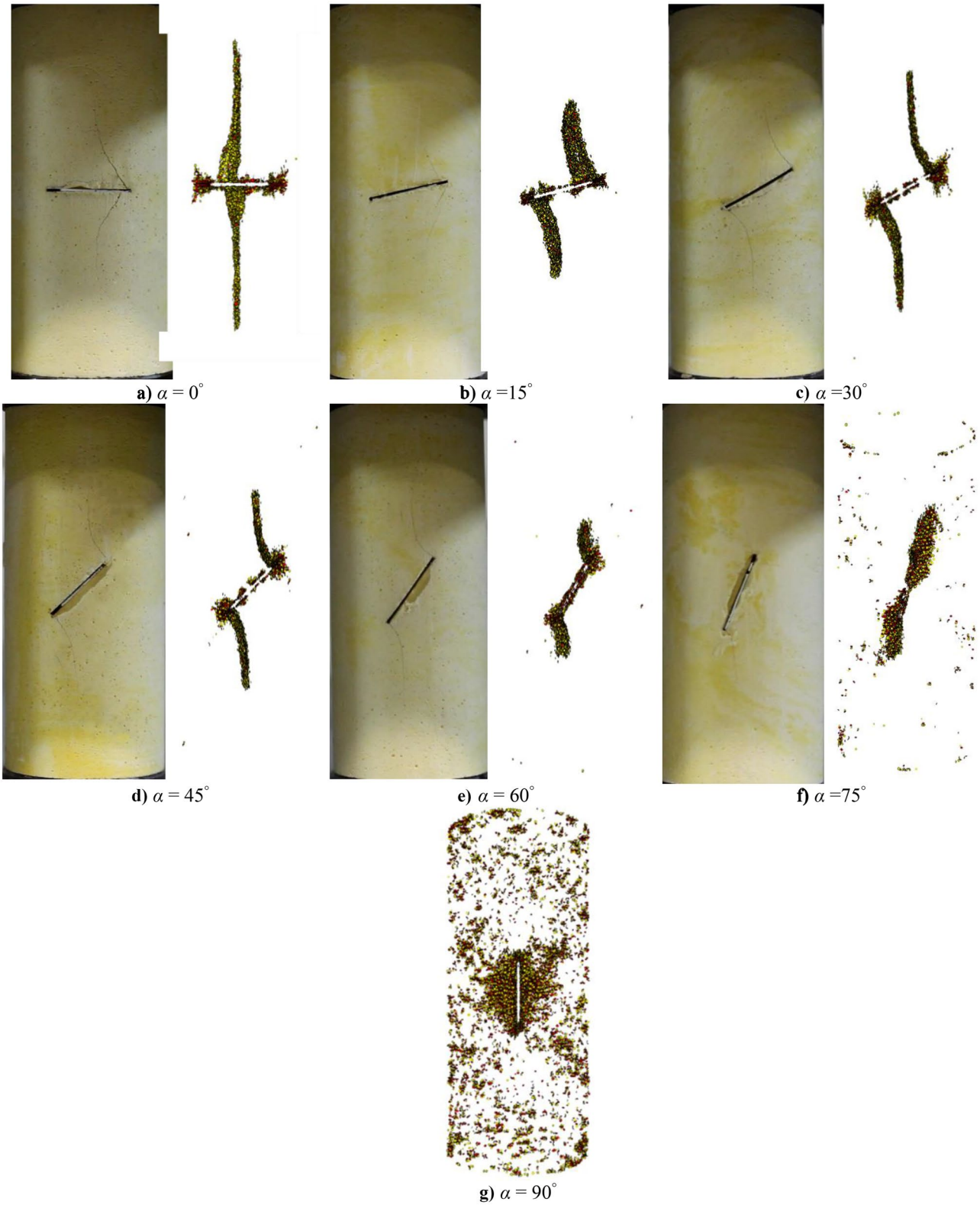

Fig. 19 The effect of flaw inclination angle on crack initiation pattern for specimens with $A = 1.2$ mm and $2a = 26$ mm

When α varies to 15°, 30°, 45°, 60°, and 75°, tensile cracks of type 1 initiate at both flaw tips in numerical and experimental models (see Figs. 22b, c, e, f; 23b, c, e, f; 24b, c, e). However, at $\alpha = 15°$ and $A = 1.2$ mm, a tensile crack initiates and propagates from the flaw's upper face near the left tip (see Fig. 22b), but this crack does not develop in the experimental model. Moreover, at $\alpha = 75°$ and $A = 2.8$ mm, in both experimental and numerical models, tensile cracks of type 3 initiate from flaw tips and grow in the axial stress direction (see Fig. 24f).

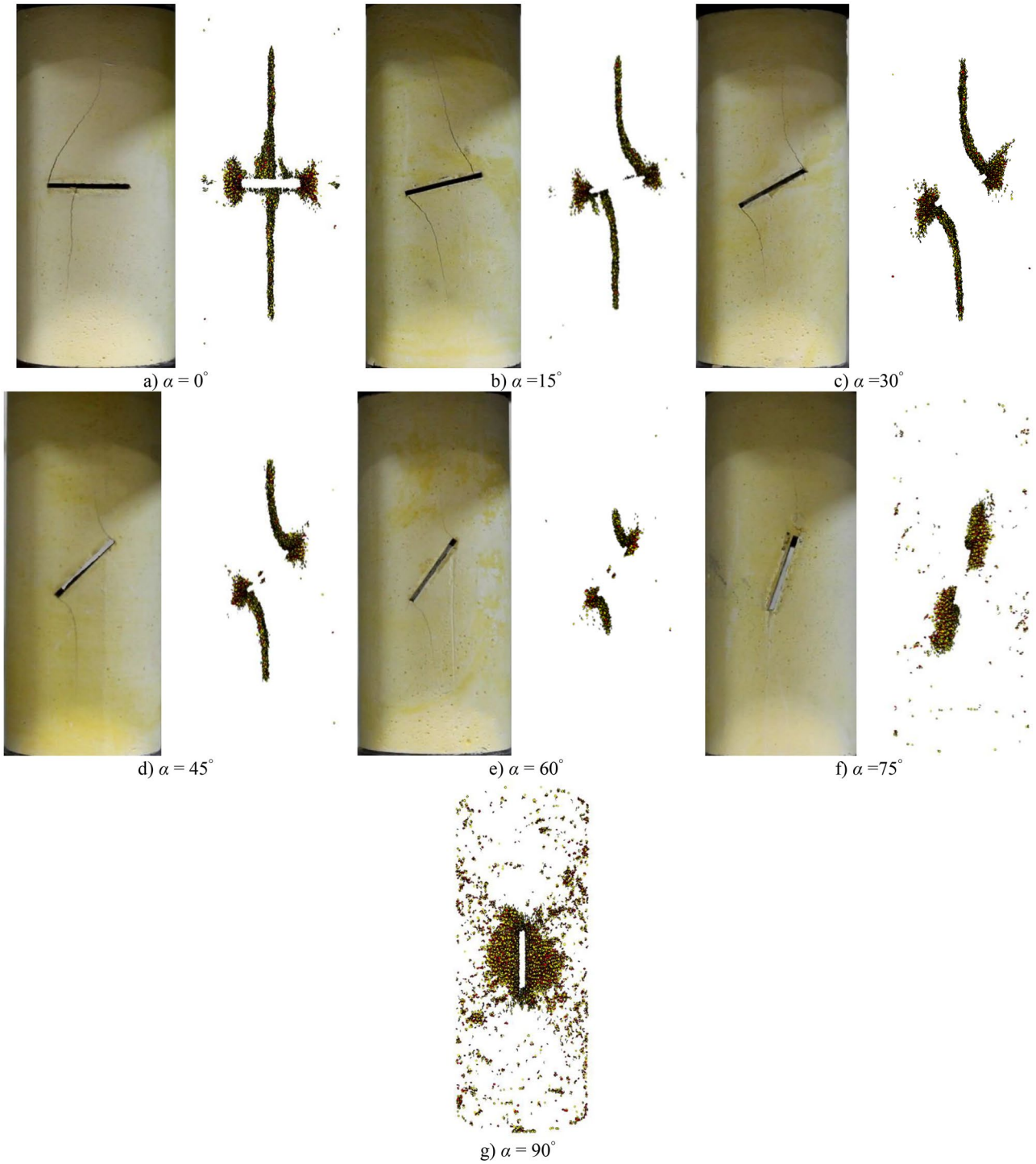

Fig. 20 The effect of flaw inclination angle on crack initiation pattern for specimens with $A = 2.0$ mm and $2a = 26$ mm

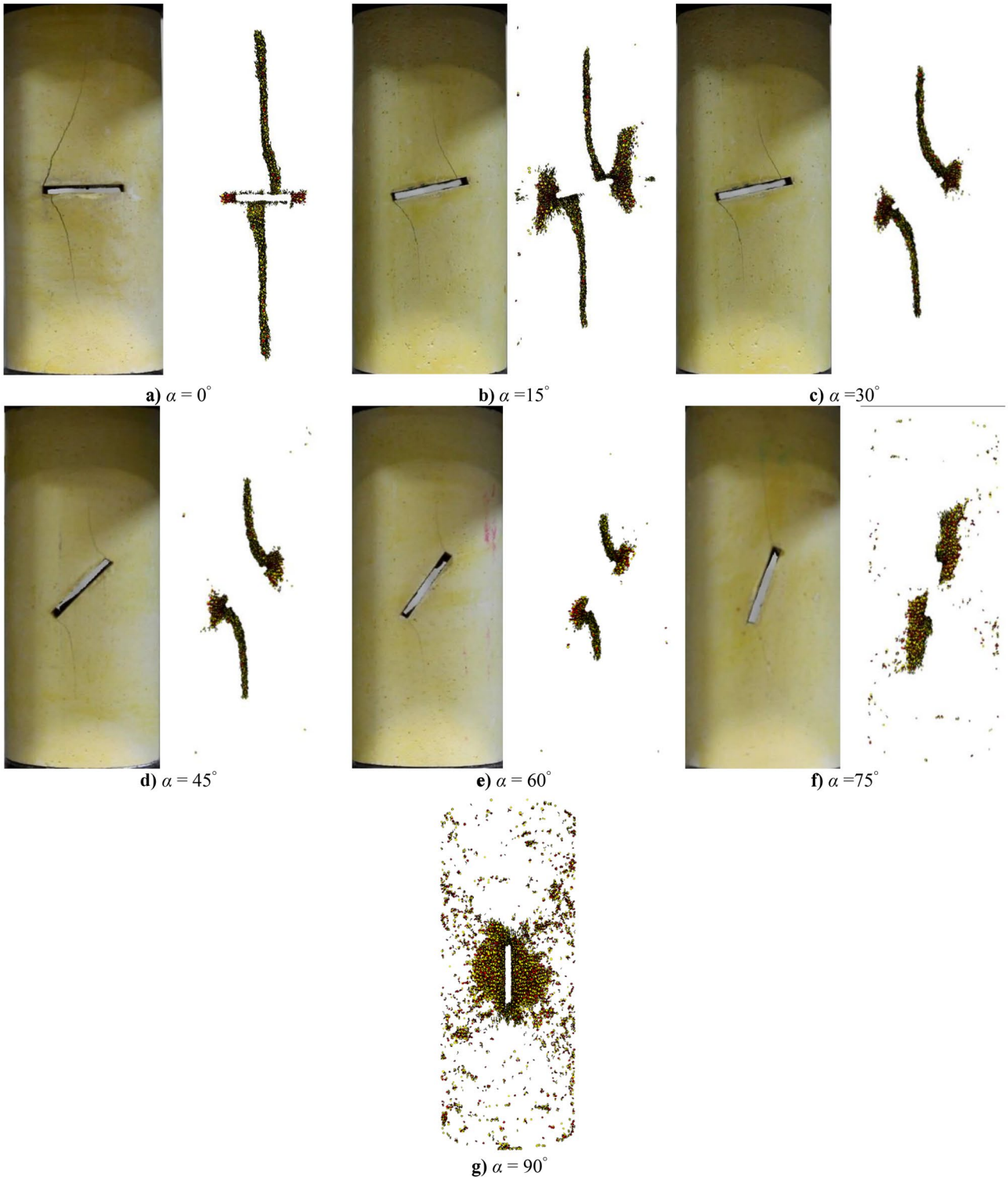

Fig. 21 The effect of flaw inclination angle on crack initiation pattern for specimens with $A = 2.8$ mm and $2a = 26$ mm

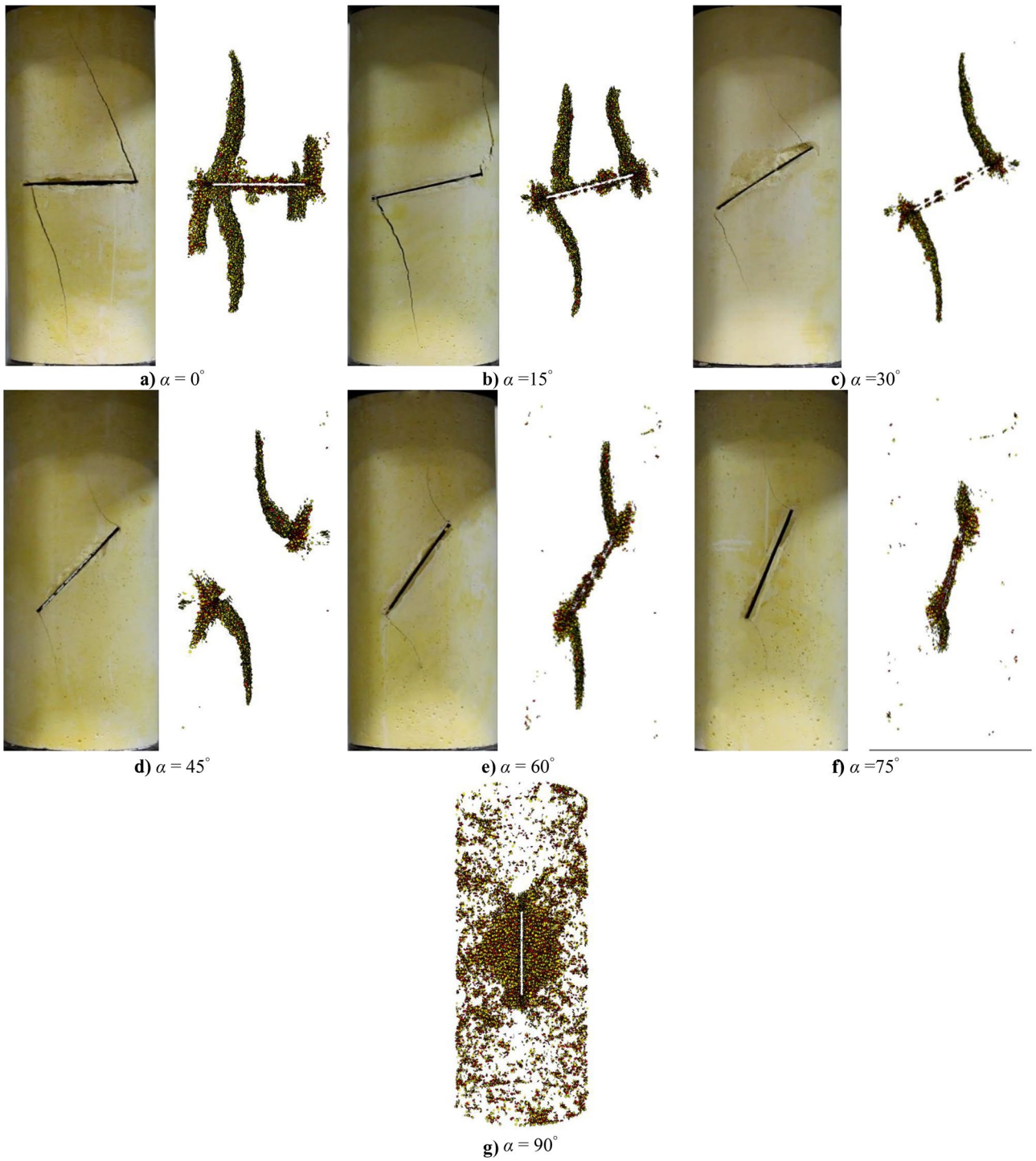

Fig. 22 The effect of flaw inclination angle on crack initiation pattern for specimens with $A = 1.2$ mm and $2a = 39$ mm

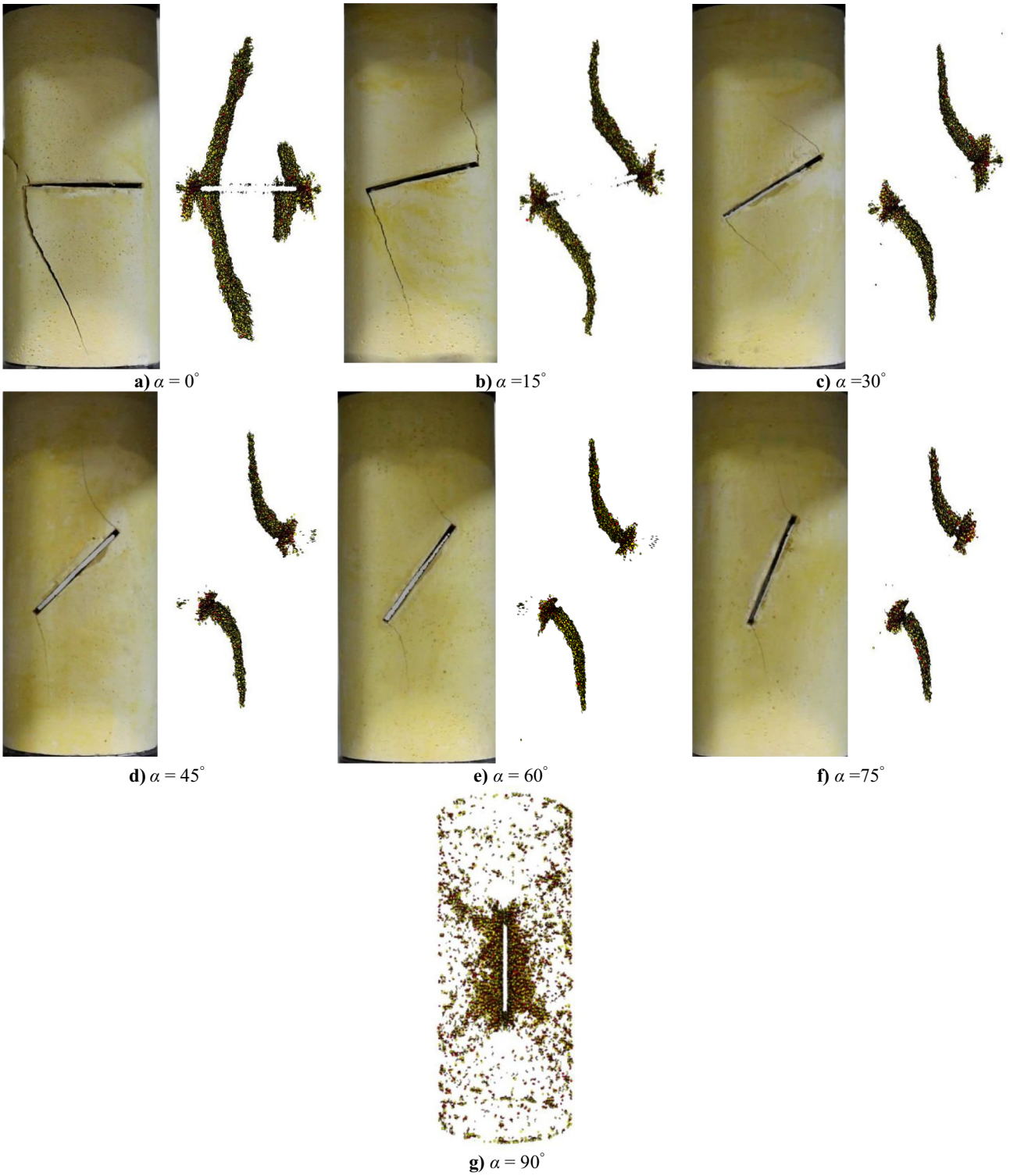

Fig. 23 The effect of flaw inclination angle on crack initiation pattern for specimens with $A = 2.0$ mm and $2a = 39$ mm

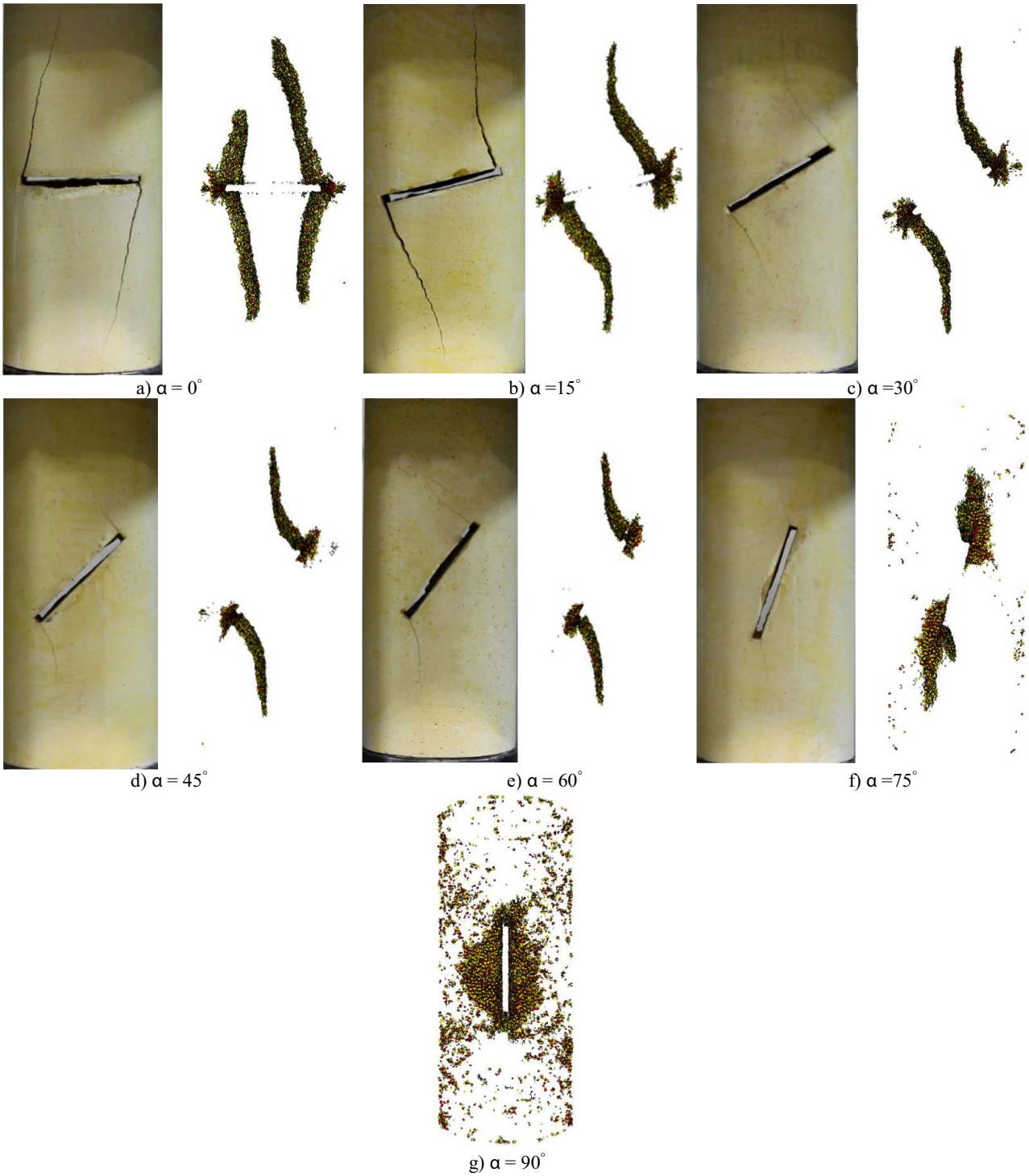

Fig. 24 The effect of flaw inclination angle on crack initiation pattern for specimens with $A = 2.8$ mm and $2a = 39$ mm

As for numerical models with $\alpha = 90°$, the crack initiation pattern is the same at different values of A in which conjugate tensile cracks initiate at flaw tips and propagate towards sample boundaries.

Conclusions

The effect of flaw angle (α), length ($2a$), and aperture (A) on strength, deformational behavior, and cracking process of single-flawed cylindrical specimens subjected to axial loading have been investigated using numerical investigations. For this purpose, 3D Particle Follow Code was adopted, and the numerical models were calibrated and verified using extensive experimental experiments (Karimi et al. 2021). The results indicate that with the increase of α at different flaw lengths and apertures, UCS and E increase. By increasing $2a$ from 13 to 39 mm at all values of α, UCS decreases, and this may happen due to stress concentration at flaw tips and impending failure of samples at higher levels of $2a$. Moreover, numerical simulations have revealed that this trend is the same for E from $\alpha = 0°$ to 60° and at $\alpha = 75°$ to 90°, flaw length virtually does not affect E. Experimental and numerical simulations have shown that A hardly affects UCS and E. The numerical analysis indicates that at $2a = 13$ and 26 mm, σ_1 at flaw tips is virtually constant up to $\alpha = 45^{\circ}$, and from this angle onward, it falls. However, at $2a = 39$ mm, σ_1 peaks at $\alpha = 45°$. When α increases and $2a = 13$ and 26 mm, σ_2 falls, and it changes to tensile at the upper flaw tip and $\alpha = 90°$. However, models with $2a = 39$ mm have a peak at $\alpha = 30°$. The numerical analysis has shown that at all apertures and $2a = 13$ and 26 mm σ_3 remains roughly stable when α ranges between 0° and 30° before experiencing a decline over the rest of the range. For models with $2a = 39$ mm, σ_3 maximize at $\alpha = 45°$. As $2a$ ranges from 13 to 39 mm, by increasing α from 0° to 60°, $\sigma 1$ decreases, and $2a$ does not affect σ_1 at $\alpha = 90°$, while it has a V-shaped trend when $\alpha = 75°$. Additionally, σ_2 peaks at $2a = 26$ mm when $\alpha \leq 75°$, and at $\alpha = 90°$, $2a$ barely impacts σ_2. Moreover, as $2a$ rises, σ_3 peaks at $2a = 26$ mm when $\alpha \leq 45°$. In models with $\alpha = 90°$ and at a lower tip of $\alpha = 60°$, σ_3 is hardly affected by flaw length, while when $\alpha = 75°$ and at the upper tip of models with $\alpha = 60°$, σ_3 experiences a rise as flaw length increases. Numerical simulations also revealed that A does not significantly affect all the principal stresses. The orientation of maximum principal stresses at the flaw tips showed that the maximum of σ_1 is in the direction axial loading (i.e., z-axis), and σ_2 is in the direction of x-axis and σ_3 in the direct of the y-axis. As for crack initiation and propagation pattern, the results of numerical and numerical investigations are in high consistency. The numerical analysis showed that increasing $2a$ initiates tensile cracks type 1 and propagates from both flaw tips. Moreover, the α significantly affects the crack patterns, and tensile crack type 1 virtually forms at α ranging from 15° to 75°, while tensile crack type 3 usually propagates at $\alpha = 0°$ and 90°. Numerical simulation showed initiation and propagation of conjugate shear cracks at flaw tips when $\alpha = 90°$; however, this failure mode needs more in-depth experimental investigations. Future work for this research involves extensive numerical studies on mechanical behavior and failure pattern of filled-single-flawed models subjected to unconfined compressive and tensile loading.

Declarations

Competing interests The authors declare no competing interests.

References

Asadizadeh M, Hossaini MF, Moosavi M et al (2019) Mechanical characterisation of jointed rock-like material with non-persistent rough joints subjected to uniaxial compression. Eng Geol 260:105224. https://doi.org/10.1016/j.enggeo.2019.105224

Asadizadeh M, Karimi J, Hossaini MF et al (2022) The effect of central flaw on the unconfined strength of rock-like specimens: an intelligent approach. Iran J Sci Technol Transact Civil Eng. https://doi.org/10.1007/s40996-022-00825-w

Asadizadeh M, Moosavi M, Hossaini MF, Masoumi H (2018) Shear strength and cracking process of non-persistent jointed rocks: an extensive experimental investigation. Rock Mech Rock Eng 51:415–428. https://doi.org/10.1007/s00603-017-1328-6

Bahaaddini M, Sharrock G, Hebblewhite BK (2013a) Numerical direct shear tests to model the shear behaviour of rock joints. Comput Geotech 51:101–115. https://doi.org/10.1016/j.compgeo.2013.02.003

Bahaaddini M, Sharrock G, Hebblewhite BK (2013b) Numerical investigation of the effect of joint geometrical parameters on the mechanical properties of a non-persistent jointed rock mass under uniaxial compression. Comput Geotech 49:206–225. https://doi.org/10.1016/j.compgeo.2012.10.012

Bieniawski ZT (1967) Mechanism of brittle fracture of rock: Part I—theory of the fracture process. Int J Rock Mech Mining Sci Geomech Abstr 4:395–406. https://doi.org/10.1016/0148-9062(67)90030-7

Bieniawski ZT (1967) Mechanism of brittle fracture of rock: Part II—experimental studies. Int J Rock Mech Mining Sci Geomech Abstr 4:407–423. https://doi.org/10.1016/0148-9062(67)90031-9

Bobet A (2000) The initiation of secondary cracks in compression. Eng Fract Mech 66:187–219. https://doi.org/10.1016/S0013-7944(00)00009-6

Bobet A, Einstein HH (1998a) Fracture coalescence in rock-type materials under uniaxial and biaxial compression. Int J Rock Mech Min Sci 35:863–888. https://doi.org/10.1016/S0148-9062(98)00005-9

Bobet A, Einstein HH (1998b) Numerical modeling of fracture coalescence in a model rock material. Int J Fract 1998b 92(3)221–252. https://doi.org/10.1023/A:1007460316400

Fan W, Yang H, Jiang X, Cao P (2021) Experimental and numerical investigation on crack mechanism of folded flawed rock-like material under uniaxial compression. Eng Geol 291:106210. https://doi.org/10.1016/j.enggeo.2021.106210

Hoek E, Martin CD (2014) Fracture initiation and propagation in intact rock – a review. J Rock Mech Geotechl Eng 6:287–300. https://doi.org/10.1016/j.jrmge.2014.06.001

Horii H, Nemat-Nasser S (1985) Compression-induced microcrack growth in brittle solids: axial splitting and shear failure. J Geophys Res: Solid Earth 90:3105–3125. https://doi.org/10.1029/JB090IB04P03105

Huang Y-H, Yang S-Q, Tian W-L, Wu S-Y (2022) Experimental and DEM study on failure behavior and stress distribution of flawed sandstone specimens under uniaxial compression. Theoret Appl Fract Mech 118:103266. https://doi.org/10.1016/j.tafmec.2022.103266

Itasca Consulting Group Inc. (2022) PFC3D manual

Jin J, Cao P, Chen Y et al (2017) Influence of single flaw on the failure process and energy mechanics of rock-like material. Comput Geotech 86:150–162. https://doi.org/10.1016/j.compgeo.2017.01.011

Karimi J, Asadizadeh M, Hossaini MF et al (2021) Compressive strength of flawed cylindrical specimens subjected to axial loading. Geomech Eng 1:87–99. https://doi.org/10.12989/gae2021.27.1.087

Li Y-P, Chen L-Z, Wang Y-H (2005) Experimental research on pre-cracked marble under compression. Int J Solids Struct 42:2505–2516

Lin H, Yang H, Wang Y et al (2019) Determination of the stress field and crack initiation angle of an open flaw tip under uniaxial compression. Theoret Appl Fract Mech 104:102358. https://doi.org/10.1016/j.tafmec.2019.102358

Liu Q, Xu J, Liu X et al (2015) The role of flaws on crack growth in rock-like material assessed by AE technique. Int J Fract 193:99–115

Manouchehrian A, Sharifzadeh M, Marji MF, Gholamnejad J (2014) A bonded particle model for analysis of the flaw orientation effect on crack propagation mechanism in brittle materials under compression. Arch Civil Mech Eng 14:40–52. https://doi.org/10.1016/j.acme.2013.05.008

Martin CD, Chandler NA (1994) The progressive fracture of Lac du Bonnet granite. Int J Rock Mech Mining Sci Geomech Abstr 31:643–659. https://doi.org/10.1016/0148-9062(94)90005-1

Mase GT, Smelser RE, Rossmann JS (1999) Continuum Mechanics for Engineers. CRC Press, New York, Second Edi

Nemat-Nasser S, Horii H (1982) Compression-induced nonplanar crack extension with application to splitting, exfoliation, and rockburst. J Geophys Res 87:6805. https://doi.org/10.1029/JB087iB08p06805

Niu Y, Zhou X-P, Berto F (2020) Evaluation of fracture mode classification in flawed red sandstone under uniaxial compression. Theoret Appl Fract Mech 107:102528. https://doi.org/10.1016/j.tafmec.2020.102528

Potyondy DO (2012) A flat-jointed bonded-particle material for hard rock. 46th US Rock Mechanics/Geomechanics Symposium 10

Shen J, Zhan S, Karakus M, Zuo J (2021) Effects of flaw width on cracking behavior of single-flawed rock specimens. Bull Eng Geol Env 80:1701–1711. https://doi.org/10.1007/s10064-020-02029-w

Sun W, Wu S, Zhou Y, Zhou J (2019) Comparison of crack processes in single-flawed rock-like material using two bonded–particle models under compression. Arab J Geosci 12:156. https://doi.org/10.1007/s12517-019-4327-y

Tang CA, Lin P, Wong RHC, Chau KT (2001a) Analysis of crack coalescence in rock-like materials containing three flaws—Part II: numerical approach. Int J Rock Mech Min Sci 38:925–939. https://doi.org/10.1016/S1365-1609(01)00065-X

Tang CAA, Lin P, Wong RHCHC, Chau KTT (2001b) Analysis of crack coalescence in rock-like materials containing three flaws—Part I: experimental approach. Int J Rock Mech Min Sci 38:925–939. https://doi.org/10.1016/S1365-1609(01)00065-X

Vaziri MR, Tavakoli H, Bahaaddini M (2022) Statistical analysis on the mechanical behaviour of non-persistent jointed rock masses using combined DEM and DFN. Bull Eng Geol Env 81:177. https://doi.org/10.1007/s10064-022-02674-3

Wang Y, Zhang H, Lin H et al (2020) Fracture behaviour of central-flawed rock plate under uniaxial compression. Theoret Appl Fract Mech 106:102503. https://doi.org/10.1016/j.tafmec.2020.102503

Wittke W (2014) Rock mechanics based on an anisotropic jointed rock model. Wilhelm Ernst & Sohn, Berlin

Wong L, Einstein H (2006) Fracturing behavior of prismatic specimens containing single flaws. Proceedings of the 41st US Rock Mechanics Symposium - ARMA's Golden Rocks 2006 - 50 Years of Rock Mechanics

Wong LNY, Einstein HH (2009) Systematic evaluation of cracking behavior in specimens containing single flaws under uniaxial compression. Int J Rock Mech Min Sci 46:239–249

Yang S-Q, Tian W-L, Huang Y-H et al (2018) Experimental and discrete element modeling on cracking behavior of sandstone containing a single oval flaw under uniaxial compression. Eng Fract Mech 194:154–174. https://doi.org/10.1016/j.engfracmech.2018.03.003

Yin P, Wong RHC, Chau KT (2014) Coalescence of two parallel pre-existing surface cracks in granite. International Journal of Rock Mechanics and Mining Sciences 68:66–84. https://doi.org/10.1016/j.ijrmms.2014.02.011

Zhang XP, Wong LNY (2012) Cracking processes in rock-like material containing a single flaw under uniaxial compression: a numerical study based on parallel bonded-particle model approach. Rock Mech Rock Eng 45:711–737. https://doi.org/10.1007/s00603-011-0176-z

Zhao C, Niu J, Zhang Q et al (2019) Failure characteristics of rock-like materials with single flaws under uniaxial compression. Bull Eng Geol Env 78:593–603. https://doi.org/10.1007/s10064-018-1379-2

Zhou XP, Cheng H, Feng YF (2014) An experimental study of crack coalescence behaviour in rock-like materials containing multiple flaws under uniaxial compression. Rock Mech Rock Eng 47:1961–1986. https://doi.org/10.1007/s00603-013-0511-7